Culture substrate stiffness impacts human myoblast contractility-dependent proliferation and nuclear envelope wrinkling

Jo Nguyen[1,2], Lu Wang[2], Wen Lei[2], Yechen Hu[3], Nitya Gulati[1,2], Carolina Chavez-Madero[1,2], Henry Ahn[4,5], Howard J. Ginsberg[4-6], Roman Krawetz[7,8], Matthias Brandt[9], Timo Betz[10], Penney M. Gilbert[1,2,11*]

[1] Institute of Biomedical Engineering, University of Toronto, Toronto, ON, Canada

[2] Donnelly Centre, University of Toronto, Toronto, ON, Canada

[3] Department of Chemistry, University of Toronto, Toronto, ON, Canada

[4] Department of Surgery, University of Toronto, Toronto, ON, Canada

[5] Li Ka Shing Knowledge Institute, Saint Michael's Hospital, Toronto, ON, Canada

[6] Department of Laboratory Medicine and Pathobiology, University of Toronto, Toronto, ON, Canada

[7] McCaig Institute, University of Calgary, Calgary, AB, Canada

[8] Department of Cell Biology and Anatomy, Cumming School of Medicine, University of Calgary, Calgary, AB, Canada

[9] Institute of Cell Biology, Center for Molecular Biology of Inflammation, University Münster, Münster, Germany

[10] Third Institute of Physics – Biophysics, Georg August University Göttingen, Göttingen, Germany

[11] Department of Cell and Systems Biology, University of Toronto, Toronto, ON, Canada

[*] Corresponding author

Email: penney.gilbert@utoronto.ca (PMG)

Abstract

The remarkable self-repair ability of skeletal muscle tissues is driven by muscle stem cells, whose activities are orchestrated by a variety of transient cues present in their microenvironment. Understanding how the cross-interactions of these biophysical and biochemical microenvironmental cues influences muscle stem cells and their progeny is crucial in strategizing remedies for pathological dysregulation of these cues in aging and disease. In this study, we investigated the cell-level influences of extracellular matrix ligands in the context of mechanically tuned culture substrates on primary human myoblast contractility and proliferation within 16 hours of plating. We found that fibronectin led to stronger stiffness-dependent responses in myoblasts compared to laminin and collagen as revealed by cell spreading area, focal adhesion morphology, traction stresses, and proliferation. While we did not observe stiffness-dependent changes in cell fate signatures at this early time-point, an analysis of the stiffness-sensitive myoblast proteome uncovered an enrichment for differentiation associated signatures on 17 kPa culture substrates, in addition to distinct profiles with relation to metabolism, cytoskeletal regulation, ECM interactions, and nuclear component enrichment. Interestingly, we found that softer substrates increased the incidence of myoblasts with a wrinkled nucleus, and that the extent of wrinkling could predict Ki67 expression. While nuclear wrinkling and Ki67 expression could be controlled by pharmacological manipulation of cellular contractility, cellular traction stresses did not correlate with nuclear envelope wrinkling level. These results provide new insights into the regulation of human myoblast stiffness-dependent contractility response by ECM ligands and also highlight a link between myoblast contractility and proliferation.

Introduction

The human skeletal muscle system sustains body mobility for many years owing to its self-repair capacity, powered by muscle stem cells (MuSCs). These MuSCs are scattered throughout muscle tissues in between muscle fibers and exist mostly in a quiescence state during homeostasis. In the event of tissue damage, MuSCs become activated, begin to proliferate, and either fuse into muscle fibers or self-renew. These processes are carefully regulated by biophysical and biochemical cues at the MuSCs residence over the tissue repair period[1,2]. MuSCs reside in a niche that is structurally polarized with the basal lamina on one side and the muscle fiber sarcolemma on the other. The basal lamina is a sheet of extracellular matrix (ECM) composed of laminins, collagens, fibronectin, and proteoglycans. During tissue repair, the ECM surrounding MuSCs can be both produced and degraded by many cell types including MuSCs themselves, causing fluctuations in its composition and physical properties like stiffness[2]. Stiffening of bulk muscle tissue and single myofibers occur upon damage[3–5], aging[4,6–9], exercise[10], and disease[11–14], while engineered niche stiffness has been shown to control myogenic cell activation[15], proliferation[4,5,16–18], differentiation[4,5,13,16,17,19], self-renewal[20], and division symmetry[21]. However, less explored is the role of specific ECM ligands in regulating stiffness-sensing in myogenic cells. Since irregular ECM remodeling is often involved in skeletal muscle aging and disease pathology, it is necessary to extend our understanding of the synergy between the physical and compositional changes in the ECM in controlling myogenic cell behavior.

MuSC adhesion to the ECM is mediated by transmembrane integrin receptors, with the most well-known being integrin α7, who together with the β1 subunit form binding receptors to niche laminin. MuSCs can also express integrins α3[22] and α6[23,24] while MuSCs progenitors in vitro express more integrin subtypes[25]. Integrin subtypes are specific to the presented ECM ligands, therefore any compositional changes in the ECM immediate to the MuSCs microenvironment hypothetically

would shift the profile of integrin subtypes recruited to the MuSCs membrane. For instance, laminin-α1 deposition has been reported to couple with the appearance of integrin α6 during MuSCs activation[24]. Since integrin subtypes can have differential binding mechanics with the ECM and thus tension-transmitting properties[26], ECM compositional dynamic not only could alter niche stiffness but potentially also how MuSCs "feel" that change. This hypothesis is challenging to test in the native MuSC niche, limited by the ability to manipulate physical niche factors without introducing chemicals disturbing the biochemical homeostasis. In vitro, murine MuSCs commitment to differentiation was reported to be sensitive to substrate stiffness on RGD-presenting hydrogels but not on laminin-presenting hydrogels[17]. MuSCs proliferation and migration have also been shown to be controlled by both ECM ligands and substrate stiffness by an unknown mechanism[17,27,28]. Deconstructing the interplay between ECM ligands and substrate stiffness converges at two questions: how ECM ligand identity changes the way myogenic cells sense substrate stiffness, and how substrate stiffness change ECM ligands signaling. In the current work, we contribute to the former question by characterizing the effects of ECM ligands on early adhesive and contractile response of myoblast to substrate stiffness, and then further emphasized the relationship between myoblast contractility and proliferation by reporting a correlation between nuclear envelope wrinkling level and Ki67 expression.

Materials and Methods

Fabrication of polyacrylamide (PAA) hydrogels

PAA hydrogels were fabricated according to the protocol described by Tse and Engler [29] with some modifications: hydrogels were cast on 35 mm glass bottom dishes (Matusunami Glass; D35-14-1-U) instead of coverslips, and deposition of NAOH was followed by immediate aspiration instead of heated evaporation. Hydrogels were then tethered with either fibronectin (Fibronectin bovine plasma, Sigma F1141), collagen (Collagen I, Rat Tail, Gibco A1048301), or laminin (Roche

98 11243217001) at a 100 mg/ml concentration according to Engler et. al. protocol. Expected
99 Young's moduli of the hydrogel formulations used in this study were extrapolated from the Engler
100 et. al. protocol (i.e., 1.10±0.34, 2.55±0.17, 4.47±1.19, 8.44±0.82, and 16.70) and were then
101 rounded to the nearest whole number: 1, 3, 5, 8, and 17 kPa, respectively, for simplicity.

102 For traction force microscopy, PAA hydrogels were fabricated following the same protocol above
103 with the addition of embedding 100 μm fluorescent beads at a 1:200 dilution.

104

105 **Primary human myoblast preparation and expansion**

106 Primary human myoblast cell lines were derived from human skeletal muscle biopsies. Four
107 primary human myoblast cell lines were used in this study: STEM21, STEM38, STEM86, and
108 UCAL38. For the STEM lines, the collection and use of the human skeletal tissues was reviewed
109 and approved by the Providence St. Joseph's and St. Michael's Healthcare Research Ethics
110 Board (REB# 13-370) and the University of Toronto Office of Research Ethics reviewed the
111 approved study and further assigned administrative approval (Protocol# 30754). Written consent
112 was obtained from donors prior to the scheduled surgical procedure. Human skeletal muscle
113 tissues removed from the multifidus muscle of patients undergoing lumbar spine surgery and
114 designated for disposal were utilized in this study. Recruitment began August 14, 2014 and ended
115 Aug 18, 2020. For the UCAL38 cell line, the collection and use of cadaveric human skeletal tissues
116 was reviewed and approved by the University of Calgary Research Ethics Board (REB# 15-0005)
117 and the University of Toronto Office of Research Ethics reviewed the approved study and further
118 assigned administrative approval (Protocol# 37165). Written consent was from next of kin.
119 Recruitment began Sept 14, 2018 and is ongoing. All procedures in this study were performed in
120 accordance with the guidelines and regulations of the respective Research Ethics Boards. Table
121 1 summarizes muscle donors' information for each line.

122

123 **Table 1. Skeletal muscle biopsy donor information**

Cell line	Donor age	Donor sex	Muscle tissue source
STEM21	64	F	Multifidus muscle of patients undergoing lumbar spine surgery
STEM38	68	M	
STEM86	60	M	
UCAL38	64	M	Gracilis muscle from cadaveric donor within 4 hours of death

124

125 The establishment of primary human myoblast cell lines was described in previous reports[30,31].
126 To summarize, human skeletal muscle biopsies were minced and incubated with collagenase
127 (Sigma, 630 U/mL) and dispase (Roche, 0.03 U/mL) in Dulbecco's Modified Eagle's medium
128 (DMEM; Gibco) to digest the ECM and basal lamina. The resulting cell slurry was then passed
129 through a 20G needle multiple times to obtain a single-cell suspension, followed by incubation
130 with red blood cell lysis buffer (Table 2). The resulting non-purified cells were plated on collagen-
131 coated tissue culture dishes for one passage in myoblast growth medium (Table 2) and then were
132 immunostained and sorted using fluorescence-activated cell sorting (FACS), to purify the CD56+
133 myogenic progenitor population.

134 Myoblasts were expanded on collagen-coated tissue culture plastic plates before being collected
135 at passage 7-8 for experiments using the following method: adherent cells were first washed with
136 pre-warmed PBS, then incubated in 0.05 % trypsin-EDTA (Thermo Fisher Scientific, 25200072)
137 at 37 °C until all cells detached (about 5 minutes). After neutralizing trypsin-EDTA with growth
138 medium, the cell solution was centrifuged in 15 ml conical tubes at 300 G for 8 minutes, then
139 resuspended in 1 ml fresh growth medium. After cell-counting using a hemocytometer, 20,000
140 cells were seeded per hydrogel (diameter=12mm) for morphology, focal adhesion analysis, and

141 traction force microscopy experiments, while 25,000 cells were seeded per hydrogel for all other
142 experiments.
143
144 **Table 2. Cell culture media and solutions**

Media and solutions	Composition
RBS lysis buffer	ddH2O, 15.5 mM NH4Cl (Sigma-Aldrich, A9434), 1 mM KHCO3 (Sigma-Aldrich, 237205), 10 μM EDTA
Growth media	Ham's F-10 Nutrient Mixture (Wisent Bioproducts, 318-050-CL), 20% FBS (Gibco, 10437028), 5 ng/ml fibroblast growth factor-2 (ImmunoTools, 11343625), and 1% penicillin-streptomycin

145

146 **ML7 and LPA treatment**

147 Prior to NE wrinkling analysis, cells were treated with 25 μM ML7 for 1 hour before fixing, or with
148 50 μM LPA for 2 hours post-seeding, followed by a wash with media before incubating cells in
149 fresh growth media until the fixation time-point. Prior to Ki67 analysis, treatment with 10 μM ML7
150 or LPA was conducted overnight. In all of these conditions, the cells were fixed at 45 hours post-
151 seeding.
152

153 **Immunostaining**

154 Fixation was done by replacing half the volume of media in the culture dish with 4 %
155 paraformaldehyde (Electron Microscopy Sciences; 15714) in phosphate buffered saline (PBS)
156 followed by a 15-minute incubation. After three 5-minute PBS washes, cells were permeabilized

157 in 0.1 % Triton-X100 (BioShop, TRX777.500)/PBS for 15 minutes. Cells were then blocked in 10
158 % goat serum in PBS for 1 hour. Immediately after blocking, primary antibodies diluted in 1 %
159 goat serum were added and left overnight at 4 °C. The following day, after three 5-minute washes
160 in 0.025 % Tween-20 (BioShop, TWN510.500)/PBS, cells were incubated in secondary antibodies
161 and Hoechst counterstain diluted in 1 % goat serum for 1 hour. For F-actin visualization, Phalloidin
162 was also added at this step. Antibodies information and dilution are reported in Table 3. Before
163 imaging, cells were washed for 5 minutes in 0.0025 % Tween-20/PBS, then a final wash on a
164 gentle shaker for 30 minutes. All steps were done at room temperature unless specified otherwise.
165 For Pax7/MyoD experiments, after the final wash, PBS was removed then a coverslip was placed
166 on top of the cells, so that imaging was done through the top coverslip with the plate upside-down
167 in case PAA hydrogels with different stiffness alter the perceived fluorescence intensity of the
168 samples, even though this has not been reported as a concern in major PAA protocols[29,32]. In
169 other experiments where fluorescence intensity was not critical, imaging was done through the
170 bottom coverslip of the glass-bottom plate.
171
172 **Table 3. Antibody information**

Antibody	Host species	Dilution ratio	Manufacturer, catalog number
Hoechst 33342	-	1:1000	Thermo Fisher Scientific, H3570
Fluorescein Phalloidin	-	1:400	Molecular Probes, F432
anti-Paxillin, clone 5H11	mouse IgG1	1:200	Millipore Sigma, 05-417

anti-Pax7	mouse IgG1	1:1	In-house supernatant from hydridoma cell line (DHSB)
anti-MyoD1	mouse IgG2b	1:300	Santa Cruz Biotechnology, sc-377460
anti-Ki67	rabbit	1:300	Abcam, ab16667
anti-Lamin A/C	mouse IgG1	1:300	Santa Cruz Biotechnology, sc-376248
anti-Lamin A/C (H-110)	rabbit	1:300	Santa Cruz Biotechnology, sc-20681
Alexafluor™ 488 Anti-mouse IgG (H+L)	goat	1:300	Invitrogen, A11001
Alexafluor™ 647 Anti-mouse IgG1	goat	1:300	Invitrogen, A21240
Alexafluor™ 546 Anti-mouse IgG (H+L)	goat	1:300	Invitrogen, A11003
Alexafluor™ 546 Anti-mouse IgG2b	goat	1:300	Invitrogen, A21141
Alexa Fluor® 647 Mouse Anti-Human CD56 (NCAM-1)	mouse IgG1	1:20	BD Pharmingen, 557711

173

174 **Traction force analysis**

175 After 16 hours of culture on PAA hydrogels with embedded fluorescent beads (ThermoFisher
176 Scientific, F8800), the cells were stained for CellTracker Deep Red dye (ThermoFisher Scientific,
177 C34565) according to manufacturer's protocol. Imaging was done in FluoroBrite DMEM
178 (ThermoFisher Scientific, A1896701), 20 % FBS (Gibco, 10437028), and 1 % penicillin-
179 streptomycin solution medium. Images of beads and cells were taken before and after the addition
180 of 10 % sodium dodecyl sulphate (SDS). Traction stress maps were obtained using ImageJ
181 macros developed in prior published work [33,34]. Using MATLAB, cell masks were obtained by
182 expanding the original CellTracker binarized image by 70 pixels in all directions. Only traction
183 stress values inside the cell masks were considered.
184

185 **EdU assay**

186 After 16 hours of culture on hydrogel substrates, cells were pulsed with EdU at a concentration of
187 1 μM for 12 hours. Cells were fixed in 4 % PFA for 15 minutes and incubated in blocking solution
188 containing 10 % goat serum and 0.3 % Triton X-100 (BioShop, TRX777) diluted in PBS for 45
189 minutes at room temperature. EdU immunolabeling was done using the Invitrogen Click-iT EdU
190 kit according to the manufacturer's protocol (Invitrogen™, C10339) and then cells were
191 counterstained with Hoechst 33342.
192

193 **Viability assay**

194 After 16 hours of culture on hydrogel substrates, cells were washed with PBS, then incubated
195 with 1 μM calcein-AM (ThermoFisher Scientific, L3224), 1 μM propidium iodide (Sigma, P4864)
196 or ethidium homodimer-1 (ThermoFisher Scientific, L3224), and 1:1000 Hoechst in PBS for 20
197 minutes at room temperature. After removing the staining solution, cells were washed with PBS
198 and imaged immediately.
199

200 **Microscopy and image analysis**

201 Except for the EdU analysis, all microscopy was done with a Zeiss Axio Observer 7 microscope
202 equipped with LSM 800 scan head. A Plan-APO 40x/NA 1.40 Oil DIC objective was used for all
203 single cell analyses (i.e. paxillin, lamin A/C, traction force microscopy, and phalloidin
204 representative images), and a Plan-Apo 10x/NA 0.45 objective was used for cell spreading area
205 and the Ki67 imaging. EdU staining images were taken using an Olympus IX83 microscope
206 equipped with a DP80 dual CCD camera and either a LUCPLFLN PH 20x/ NA 0.46 or UPLFLN
207 2PH 10x/ NA 0.3 objective.
208 All image analysis was performed with ImageJ. FA alignment by goodness of fit (GoF) to a
209 Gaussian curve was obtained by running the Directionality ImageJ plug-in (written by Jean-Yves
210 Tinevez; https://imagej.net/plugins/directionality) on a random region of interest (ROI) close to the
211 cell periphery on the maximum projection of paxillin z-stacks. The analysis performed was based
212 on Fourier spectrum analysis. The percentage of total cells labeled by EdU was quantified by
213 dividing the number of segmented objects in the EdU channel by the number of segmented
214 objects in Hoechst channel. Nuclear wrinkling index was quantified using the ImageJ macro
215 developed by Cosgrove et. al [35] with some adjustments to allow semi-batch processing of our
216 datasets. The adapted macro used can be found in our public Github repository
217 (https://github.com/gilbertlabcode/Nguyen_PLOS_One2023). Ki67, Pax7, and MyoD
218 fluorescence intensities in each cell were quantified by measuring the integrated density inside
219 each nucleus. Binary binning (+/-) of Ki67, Pax7, and MyoD was done by identifying an intensity
220 threshold below which cells appear “negative” by reference to the secondary antibody controls.
221

222 **Lentiviral production**

223 Lentivirus particles were produced by calcium phosphate transfection, as reported previously[36].
224 Briefly, 35,000/cm^2 HEK 293T cells were seeded in a 10-cm culture plate and co-transfected 2
225 days later at 80 % confluency with second generation lentivirus system. Culture media (DMEM
226 supplemented with 10 % FBS) was refreshed prior to transfection, followed by addition of the

227 plasmid cocktail containing 4 µg of pMD2.G (a gift from Didier Trono; Addgene plasmid # 12259;
228 http://n2t.net/addgene:12259; RRID:Addgene_12259), 10 µg of psPAX2 (a gift from Didier Trono;
229 Addgene plasmid # 12260; http://n2t.net/addgene:12260; RRID:Addgene_12260) and 15 µg of
230 pLVX-EF1a-GFP-LaminA-IRES-Hygromycin [37] (a gift from David Andrews; Addgene plasmid #
231 134867; http://n2t.net/addgene:134867; RRID:Addgene_134867) for 12 hours. Culture media
232 was replaced to OptiMEM (Thermofisher, 31985062) 20mM HEPES (Sigma-Aldrich, 51558-
233 50ML), and the supernatant containing viral particles was collected at 24 and 48 hours after
234 transfection, passed through a 0.45 µm filter, and then concentrated using a 50 mL 100 000
235 MWCO spin column (Cytiva Life Sciences).
236
237 **Lentiviral transduction**
238 Primary human myoblasts were plated in a collagen-coated 6-well plate in growth media and
239 transduced when the cells were at about 50% confluency (i.e. ~ 24 hours after plating). 150-500
240 µL of viral supernatant containing 6 µg/mL polybrene (EMD Millipore, TR-1003-G) and was added
241 dropwise to the cells in fresh growth media and then incubated for 12 hours. The virus containing
242 media was aspirated and the cells were returned to regular growth media for 48 hours. The cells
243 were then trypsinized and seeded onto 17 kPa hydrogel substrates for 16 hours until traction force
244 microscopy experiment.
245
246 **Proteomics**
247 *Reagents*
248 Trypsin from bovine pancreas (Promega Biotec, V5113), lysine-C (New England BioLabs,
249 P8109S), protease and phosphatase inhibitor cocktail (ThermoFisher Scientific, 78442), formic
250 acid (FA, Sigma–Aldrich, F0507-100ML), tris(2-carboxyethyl) phosphine (TCEP, Sigma–Aldrich ,
251 C4706-2G), iodoacetamide (IAA, Sigma–Aldrich, I1149-5G), acetonitrile (≥ 99.9 %, CAN, Fisher
252 Chemicals, A9551), and water (Fisher Chemicals, W6-4).

253

254 *Preparation and digestion of protein extracts from myoblasts*

255 Myoblasts cultured on hydrogel substrates for 45 hours were collected by incubation with trypLE™
256 (ThermoFisher Scientific, 12604013). Cell numbers were determined by hemocytometer
257 counting. For each stiffness condition, a total number of 100,000 cells were washed three times
258 with cold PBS and resuspended in 20 µl lysis buffer (50 mM PBS, 1 % (v/v) protease inhibitor
259 cocktail). After three continuous freezing and defrost cycles, insoluble portions were separated
260 from the soluble portions by centrifugation at 16,000 × g for 20 minutes at 4 °C. Samples were
261 reduced in 10 mM TCEP (final concentration) at 70 °C for 30 minutes, alkylated with 20 mM IAA
262 (final concentration) in the dark at room temperature for 30 minutes, followed by incubation with
263 lysine-C (1:60) at 37 °C for 1.5 hr. Trypsin (1: 25) was then added and incubated at 37 °C for 16
264 hr. Finally, digests were quenched by the addition of 1 µL of concentrated formic acid.

265

266 *NanoRPLC-ESI-MS/MS methods*

267 Nanoflow reversed-phase liquid chromatography (NanoRPLC) was performed on an EASY-nLC
268 1200 ultra-high-pressure system coupled to a Q-Exactive HF-X mass spectrometer equipped with
269 a nano-electrospray ion source (Thermo Fisher Scientific). The obtained peptides were
270 automatically loaded onto a C18 trap column (100 µm i.d. × 5 cm) and separated by a C18
271 capillary column (100 µm i.d. × 15 cm). The trap column and the analytical column were both
272 packed in-house with 1.9 µm, 120 Å ReproSil-Pur C18 reversed phase particles (Dr. Maisch
273 GmbH). Two mobile phases (A: 0.1 % (v/v) FA and B: 80/20/0.1% ACN/water/formic acid (v/v/v)
274 were used to generate a 130 minutes gradient with the flow rate of 300 nL/minute (kept at 3 % B
275 for 5 minutes, 90 minutes from 3 % to 30 % B, 20 minutes from 30 % to 45 % B, 1 minutes from
276 45 % to 95 % B and 14 minutes to kept at 95 % B). MS was operated in full scan (120,000 FWHM,
277 400-1100 m/z) and data-independent acquisition (DIA) modes at positive ion mode. A 25.0 m/z
278 isolation window was set for MS/MS scan (60,000 FWHM) with stepped HCD collision energy of

279 25.5 %, 27 % and 30 %. The maximum IT for both MS and MS/MS was 254 ms. The electro-
280 spray voltage was 2.0 kV, and the heated capillary temperature was 275 °C. All the mass spectra
281 were recorded with Xcalibur software (version 4.1, Thermo Fisher Scientific).
282
283 *Database search*
284 DIA-NN 1.8 were applied for database searching against the Uniprot_Homo Sapiens database
285 (updated on 11/11/2021, 78120 entries) and the predicted spectrum library. The predicted
286 spectrum library was generated by DIA-NN 1.8 using the same database. The parameters of
287 database searching include up to one missed cleavage allowed for full tryptic digestion, precursor
288 ion mass tolerance and product ion mass tolerance were set 10 and 20 ppm, respectively,
289 carbamidomethylation (C) as a fixed modification, and oxidation(M), acetyl (protein N-term) as
290 variable modifications. Match between runs (MBR) was activated. Peptide spectral matches
291 (PSM) were validated based on q-value at a 1 % false discovery rate (FDR).
292
293 *Data processing*
294 Overrepresentation tests were done with PANTHER database version 17.0 released on 2022-02-
295 22 using Fisher's exact test with false discovery rate correction. For PANTHER pathways
296 annotation, the input was a list of differentially regulated proteins in both directions. For GO
297 cellular component annotation, the inputs were upregulated proteins in either soft or stiff
298 conditions.
299
300 **Data normalization**
301 Cell spreading area: Cell area data had a log-normal distribution (S1 A-B Fig). To meet the
302 normality assumption underlying the ANOVA test to compare the means between substrate
303 conditions, analysis was done based on the natural log of cell area (ln(Area)). Additionally, our
304 experiments were repeated on primary human myoblasts lines from independent donors. To

minimize cell line variance that may mask substrate effects, we normalized the mean ln(Area) values to that of the values obtained on the 9 kPa condition for each cell line: normalized ln(Area) = ln(Area)/ln(Area)$_{8kPa}$. Pre-normalized data is reported in S1 C-E Fig.

EdU assay: aside from reporting the unadjusted data, we scaled each cell line by the maximum % total EdU+ value (scaled $x = x/x_{max}$) before linear regression fitting. Normalization by scaling allowed us to focus on comparing the stiffness-dependent trends and minimized cell line variance in the exact values of % total EdU+ cells.

Statistical analysis

All statistical analysis was conducted using GraphPad Prism 6.0 software. To compare two conditions in experiments with one independent variable, comparisons were done with t-tests. To compare more than two conditions in experiments with one independent variable, a one-way ANOVA test preceded Holm-Šídák multiple comparison tests. For experiments with two independent variables, two-way ANOVA preceded Holm-Šídák multiple comparison tests. For all tests, α=0.05. p-values used to discuss comparisons between conditions are reported on top of graphs.

Table 4. Experimental replicate breakdown and statistical analysis

Figure	Cell number n and biological replicates N	Sample size n used for statistical analysis and error bars	Statistical analysis
1B	FN 1 kPa: n=515 FN 3 kPa: n=395 FN 5 kPa: n=548 FN 8 kPa: n=594	n=3 from each condition	two-way ANOVA followed by Tukey's multiple comparison tests

	FN 17 kPa: n=601 LAM 1 kPa: n=567 LAM 3 kPa: n=471 LAM 5 kPa: n=414 LAM 8 kPa: n=455 LAM 17 kPa: n=445 COL 1 kPa: n=920 COL 3 kPa: n=835 COL 5 kPa: n=884 COL 8 kPa: n=678 COL 17 kPa: n=899 from N=3.		
2C	FN 1 kPa: 32 FN 3 kPa: 28 FN 17 kPa: 26 LAM 1 kPa: 30 LAM 3 kPa: 30 LAM 17 kPa: 30 COL 1 kPa: 27 COL 3 kPa: 28 COL 17 kPa: 29 from N=3.	n=3 from each condition	two-way ANOVA followed by Holm-Šídák multiple comparisons tests
3B, 3C	FN 3 kPa: 22 FN 17 kPa: 20 LAM 3 kPa: 19	n=3 from each condition	two-way ANOVA followed by a Holm-

	LAM 17 kPa: 21 COL 3 kPa: 24 COL 17 kPa: 22 from N=3.		Šídák multiple comparison test
4B	FN 1 kPa: 691 FN 3 kPa: 923 FN 17 kPa: 655 LAM 1 kPa: 751 LAM 3 kPa: 854 LAM 17 kPa: 462 COL 1 kPa: 698 COL 3 kPa: 828 COL 17 kPa: 715 from N=3.	n=3 from each condition	two-way ANOVA followed by a Holm-Šídák multiple comparison test
4C	FN 1 kPa: 691 FN 3 kPa: 923 FN 17 kPa: 655 LAM 1 kPa: 751 LAM 3 kPa: 854 LAM 17 kPa: 462 COL 1 kPa: 698 COL 3 kPa: 828 COL 17 kPa: 715 from N=3.	n=3 from each condition	Linear regression

6B	Soft: 149 Stiff: 121 from N=3.	n=5 from each condition	one-way ANOVA followed by a Holm-Šídák multiple comparison test
6C	Soft: 105 Stiff: 75 from N=3.	N/A	No statistical analysis
6D	Soft: 105 Stiff: 75 from N=3.	n=3 from each condition	paired one-tail t-test
7B	Soft+DMSO: n=106 Stiff+DMSO: n=74 Stiff+ML7: n=78 from N=3.	n=3 from each condition	one-way ANOVA followed by a Holm-Šídák multiple comparison test
7C	Soft+DMSO: n=60 Stiff+DMSO: n=72 Soft+LPA: n=63 from N=3.	n=3 from each condition	one-way ANOVA followed by a Holm-Šídák multiple comparison test
7D	Soft+DMSO: n=1060 Stiff+DMSO: n=726 Stiff+ML7: n=657 Soft+LPA: n=688 from N=3.	n=3 from each condition	one-way ANOVA followed by a Holm-Šídák multiple comparison test
S3 Fig	Soft: 435 Stiff: 469	n=3 from each condition	

	from N=3.		

Representative image preparation

Figure 1: Cropped images were placed on a black background separated by white lines. Images were max projection of z-stacks.

Figure 2: Raw paxillin staining images were processed according to a published process [38] up to the Log3D filtering step to create representative images. These images were then processed with the Log3D plug-in, binarized, and cropped to create the insets.

Figure 3: Filtered stress maps were created following the process written in the “Traction force analysis” section above.

Figure 4: The brightness and contrast of raw EdU and Hoechst images were equally adjusted in all conditions.

Figure 5: Individual nuclei were cropped from raw Lamin A/C images. The brightness and contrast of Lamin A/C were equally adjusted for all nuclei.

Figure 6: Images from the first three conditions (soft+DMSO, stiff+DMSO, stiff+ML7) were collected from the same experiment so their brightness and contrast were adjusted equally. The images for the soft+LPA condition were collected from a separate experiment, and thus, the brightness and contrast were adjusted to most closely match that of the other conditions. Note that fluorescence intensity was not considered in the analysis of these results.

Results

Accentuated myoblast stiffness sensitivity observed on fibronectin-tethered substrates

We first explored the influence of ECM ligand tethering on human primary myoblast responses associated with stiffness-sensing that included cell spreading area, focal adhesion assembly, and

346 traction stress. We followed a well-established poly-acrylamide (PA) hydrogel fabrication protocol
347 to create cell culture substrates with tuned stiffness that we then tethered with ECM ligands found
348 within the native muscle stem and progenitor cell microenvironment: fibronectin (FN), laminin
349 (LAM), or collagen-1 (COL)[29]. We selected PA gel stiffnesses of 1, 3, 5, 8, and 17 kPa to mimic
350 the reported range of the Young's modulus of skeletal muscle and single muscle fibers, which
351 were reported to be approximately 0.2-18 kPa, spanning healthy, damaged, and aged states
352 [4,13,20,21,39,40].

353 16 hours after plating on FN substrates, human primary myoblast cell spreading was minimal on
354 1 kPa culture substrates, noticeably increased at 3kPa, then plateaued from 3 to 17 kPa (Fig 1).
355 Cell spreading on LAM substrates presented a similar relationship with culture substrate stiffness,
356 although a slight decrease in spreading at 17 kPa was observed. By contrast, cells on COL
357 substrates attained equally large spreading area independent of culture substrate stiffness within
358 the tested stiffness range, except for a decrease at 17 kPa (Fig 1A-B). As we only included well
359 isolated mononucleated cells in our analysis, the decrease in spreading area at 17 kPa may have
360 been an analysis artifact due to the greater likelihood of larger cells making physical contact with
361 neighboring cells.

362 Next, we visualized adhesion structures with paxillin immunostaining and noted that the paxillin
363 structures detected had a broad range of sizes (Fig 2A). On the 1 kPa substrates tethered with
364 FN and LAM, wherein the myoblasts had minimal spreading, we observed long paxillin+ structures
365 outlining the nucleus and/or the peripheral edges of the cells. The appearance of cells with these
366 features was rare on the higher substrate stiffnesses and were also rare on the COL tethered
367 substrates more generally. Adhesion structure morphologies varied along three scales: within a
368 single cell, across different cells cultured on the same substrates, and between the biological
369 replicate cell lines. These variabilities made it challenging to attribute substrate effects to adhesion
370 size and shape, which, by themselves, are insufficient to infer focal adhesion function and maturity

371 [41]. For this reason, we instead chose to quantify local adhesion structure alignment. Since cells
372 exert traction forces through adhesion structures where stress fibers terminate, the alignment of
373 adhesion structures is indicative of the alignment of stress fibers and provides a speculative
374 imagery of the cell contractility state[42,43]. To measure the alignment of adhesion structures, we
375 used the "Directionality" ImageJ plugin, which generates a frequency distribution histogram of
376 structures over a range of direction angles (with 0° being the East direction and going
377 counterclockwise). The histogram was then fitted to a Gaussian curve. If the structures in the
378 region of interest align in a common direction, the histogram will have a peak and resemble a
379 Gaussian curve, thus having a high goodness of fit (GoF) (Fig 2B, top). Conversely, if a common
380 direction of alignment does not exist, the histogram will be flat and have a low GoF (Fig 2B,
381 bottom). The alignment of paxillin structures across substrate conditions showed trends like the
382 cell spreading area data (Fig 1). Specifically, on FN and LAM substrates, GoF was low at 1kPa,
383 increased at 3kPa and then remained relatively constant at 17kPa, although the increase on LAM
384 substrates was more subtle, and did not reach statistical significance in our study (Fig 2C). On
385 the COL substrates, adhesion structures reached equally high alignment regardless of substrate
386 stiffness (Fig 2C).

387 Although cell spreading area and adhesion alignment did not differ significantly between 3 and 17
388 kPa on FN substrates, upon conducting traction force microscopy studies, we observed a
389 significant increase in mean and max traction stress across these conditions. Similar trends were
390 seen on the LAM and COL substrates, though the magnitude of the effect was more subtle than
391 on the FN condition (Fig 3A-C).Traction data on 1 kPa substrates were excluded from this analysis
392 because we were unable to reliably derive cellular traction stress with our workflow because of
393 the extremely large hydrogel deformations. Likely due to large deformation caused on softer
394 hydrogels, even though lower stresses were recorded on 3 kPa substrates compared to 17 kPa,

395 strain energy was generally higher on 3 kPa than 17 kPa in all ECM conditions, but was only
396 statistically significant for COL (S3 Fig).

397 In summary, by evaluating the morphology, focal adhesion arrangement, and cellular traction
398 stress of primary human myoblasts cultured on 1, 3, and 17kPa PA hydrogels, we found that FN-
399 tethered hydrogel substrates encouraged more pronounced stiffness sensitivity when compared
400 against the LAM- and COL- tethered substrates, in terms of the above metrics.

401 **ECM ligands influence the linearity of proliferation correlation with substrate stiffness**

402 To probe whether ECM ligands also tune cellular functional response to substrate stiffness, we
403 evaluated myoblast proliferation using the 5-ethynyl-2'-deoxyuridine (EdU) assay. After cells were
404 cultured for 16 hours on hydrogel substrates, we added EdU in the culture media for 12 hours.
405 The percentage of EdU+ cells increased steadily from 1 to 17 kPa for myoblasts cultured on FN-
406 tethered substrates (Fig 4B). For LAM- and COL-tethered substrates, the percentage of EdU+
407 cells showed an insignificant, trended increase from 1 to 3 kPa and then remained constant from
408 3 to 17 kPa. We suspected that myoblast proliferation and substrate stiffness had a positive, linear
409 correlation on FN but not on LAM and COL substrates. To assess linearity, we scaled %EdU+
410 values to minimize cell line variance while maintaining the correlation slope (refer to Methods)
411 then performed linear regression fitting. On FN substrates, %EdU+ cells and substrate stiffness
412 were indeed linearly fitted with an r^2=0.7 while LAM and COL were poorly linear with r^2 values of
413 0.3 and 0.2 respectively. The correlation slope in FN condition was also significantly non-zero
414 with p=0.007 while p-values for LAM and COL were higher at 0.160 and 0.291 (Fig 4C). To
415 eliminate the possibility that non-proliferative cells were instead undergoing apoptosis, we
416 performed a live/dead assay, whose result indicated that all cells across all stiffnesses on FN-
417 tethered substrates were calcein-AM positive and propidium iodide negative (S2 Fig).

418

419 **Nuclear envelope (NE) wrinkling can predict Ki67 expression**

420 In conducting EdU analysis, we noticed qualitatively that there were more cell nuclei with odd
421 shapes on softer substrates, so we asked if NE morphology regulation could be upstream of
422 stiffness-dependent proliferation control. We followed through with a series of experiments
423 focusing on two conditions: soft (1kPa) and stiff (17kPa) FN substrates. Immunostaining for Lamin
424 A/C revealed a heterogeneity in NE shapes on both stiffnesses: some nuclei were taut and oval-
425 like, as generally expected for adherent cells, but some were severely wrinkled (Fig 5A). We
426 quantified NE wrinkling by measuring wrinkle index (WI) using an ImageJ macro developed by
427 Cosgrove et al. with minor modifications[35]. We found that taut nuclei with no or minor folding
428 have WI ≤ 20%, whereas wrinkled nuclei have WI > 20%. Noticeably, the percentages of wrinkled
429 nuclei, defined by WI > 20%, were two times higher on soft compared to stiff FN-tethered
430 substrates (around 40% and 19%, respectively).
431 We further plotted Ki67 intensity against the WI of each cell in each stiffness condition. Ki67
432 intensity levels were either negative, low positive (cells in active cell cycle but not S-phase), or
433 high positive (cells in S-phase)[44]. We observed that although a taut nucleus did not always have
434 high Ki67 intensity, a nucleus with high Ki67 intensity was always taut (WI ≤ 20%), at least in the
435 three cell lines studied (Fig 5C). Wrinkled nuclei were four times less likely than taut nuclei to be
436 Ki67+ at any intensity (Fig 5D).

437 In summary, there were higher incidences of wrinkled nuclei when myoblasts were cultured on
438 soft substrates, and myoblasts with wrinkled nuclei did not express high levels of Ki67.

439 **Pharmacological manipulation of contractility modulates NE wrinkling level and myoblast**
440 **proliferation**

441 Cellular contractile force is transmitted by actin retrograde flow from adhesion sites towards the
442 cell center, where the cytoskeleton is directly linked to the nucleus[45–47]. To investigate if low
443 contractility on soft substrates causes NE wrinkling in myoblasts, as has been observed in
444 mesenchymal stromal cells (MSCs)[35], we mirrored established methods to pharmacologically

445 inhibit and activate cellular contractility using a myosin light chain kinase inhibitor (ML7) and
446 lysophosphatidic acid (LPA), respectively. Consistent with MSCs studies, we found that ML7
447 treatment increased the percentage of wrinkled nuclei on stiff substrates, while LPA treatment
448 lowered the incidence of wrinkled nuclei on soft substrates, although the effect was not as
449 pronounced as ML7 (Fig 6A-C). Additionally, overnight treatments of ML7 decreased the
450 proportion of Ki67+ myoblasts present on stiff culture substrates, while LPA increased Ki67+
451 proportion on soft substrates (Fig 6D).

452 With these results, we hypothesized that cellular traction stresses would be lower in cells with
453 wrinkled nuclei (WI > 20) compared to cells with taut nuclei (WI ≤ 20%). To test this hypothesis,
454 we conducted traction force microscopy on myoblasts cultured on 17 kPa FN substrates
455 expressing a live Lamin A reporter, the pLVX-EF1a-GFP-LaminA-IRES-Hygromycin plasmid [37].
456 Unexpectedly, traction stresses and strain energy values were similar between cells with taut and
457 wrinkled nuclei (Fig 6 E-G, S4 Fig). This suggests that the relationship between cellular
458 contractility and NE wrinkling is not straightforward. It is possible that cells with wrinkled nuclei on
459 1 kPa substrates had lower traction stresses than those on 17 kPa. But if low contractility was the
460 only cause of NE wrinkling, a negative correlation between contractility and WI would have been
461 observed among cells on the same substrate stiffness.

462 In summary, it appears that pharmacological manipulation of cellular contractility can alter NE
463 wrinkling, and the absence of NE wrinkling seems to be a prerequisite for high Ki67 expression in
464 myoblasts. However, low cellular contractility is likely not the only cause of NE wrinkling.

465 **Proteomic assessment of myoblast cellular processes and fate**

466 To gain a comprehensive understanding of cellular processes following the initial responses to
467 substrate stiffness, we profiled the proteomes of 100,000 cells cultured for 45 hours on either 1
468 or 17 kPa FN-tethered substrates, between which we saw the most distinct differences in cellular-
469 level responses. We will refer to these conditions as “soft” and “stiff” substrates in subsequent

470 discussions. 100,000 cells in each stiffness condition were split into three technical replicates. All
471 proteomic data and analysis are provided in the supporting information.

472 Over 3216 protein groups were detected across the three technical replicates, and only groups
473 with quantitative information in at least 2 out of the 3 replicates were considered. Myoblasts
474 cultured on soft and stiff substrates had distinguishable proteomic profiles (S5A Fig). Among
475 these filtered protein groups, 838 were determined to be differentially expressed by a $p < 0.05$
476 cut-off (S5B Fig). Using the PANTHER database to analyze differentially expressed proteins, we
477 identified 5 enriched pathways: pentose phosphate pathway, glycolysis, integrin signaling
478 pathway, cytoskeletal regulation by Rho GTPase, and Huntington disease (Fig 7A). The
479 enrichment of integrin signaling and cytoskeletal regulation by Rho GTPase are expected in the
480 context of adherent cell stiffness-sensing. Cancer cells cultured on soft environments have been
481 reported to have reduced metabolic activities which may play a role in decreasing proliferation
482 rate[48]. With the top two overrepresented pathways in our proteomic analysis being pentose
483 phosphate pathway and glycolysis, we further looked at the expression of components of these
484 metabolic pathways, and ATP synthases, for evidence of myoblasts potentially being
485 metabolically dormant on soft substrate. Many enzymes catalyzing chemical processes in
486 pentose phosphate pathway and glycolysis were detected to have been more abundant on soft
487 substrates, and ATP synthase subunits expressions had mixed correlation with substrate stiffness
488 (S6A-B Fig). Without measuring direct metabolic outputs such as ATP levels, whether there was
489 a metabolic halt on soft substrates remained a standing question, but our proteomic assessment
490 suggests that if there was a halt, it likely would not have been due to the lack of metabolic enzymes
491 or ATP synthase.

492 Myogenic proliferation and differentiation are regulated by a series of transcription factor activities.
493 In vitro, myoblast fate signatures are often profiled by assessing expression of the transcription
494 factors Pax7 and MyoD: Pax7+/MyoD- (stem-like or reserve-like cells), Pax7+/MyoD+

495 (proliferative cells), and Pax7-/MyoD+ (differentiating cells). We asked whether there was an
496 increase in the proportion of either reserve-like or differentiating cells that might have
497 corresponded to the larger portion of non-proliferative cells observed on soft culture substrates.
498 We found that the proportions of fate signatures were similar on both stiffnesses, with most cells
499 being Pax7+/MyoD+ (S7A-B Fig). Interestingly, the proteomics data reported an overall lower
500 MyoD expression for myoblasts cultured on soft substrates (Fig 7B), while desmin, a myogenic
501 commitment marker, was expressed at a higher level on stiff substrate (Fig 7B). Furthermore,
502 JUNB, which has been previously reported to suppress myogenin expression[49], was found to
503 express at a higher level on soft substrate (Fig 5 B). Our immunocytochemical analysis suggests
504 that there may not have been a major divergence in the Pax7/MyoD myogenic fate landscape
505 across the two substrate stiffness levels at the 45-hour time-point post-seeding in growth medium.
506 However, based upon the proteomics assessment a stiff substrate at 17 kPa would favor a more
507 differentiative phenotype while soft substrate would favor a more reserve-like phenotype. To
508 significantly cultivate these fate transitions, we expect that other factors like culture time and
509 medium composition would need to be redesigned.

510 We noticed higher expressions of ECM proteins like FN1, several COL alpha units, and LAMC1
511 in cells on soft substrate (Fig 7D), which could suggest that myoblasts were actively attempting
512 to modify their environment thus not being completely inactive on soft substrate.

513 We also performed gene ontology (GO) overrepresentation tests on proteins upregulated in either
514 soft or stiff condition. For these tests, we further filtered differentially expressed proteins by their
515 fold change (stiff/soft). Only proteins with fold change less than or equal to 0.9, or more than or
516 equal to 1.1 were considered. Among the top five enriched cellular components in either stiffness
517 were several nuclear components (Fig 7E). LMNA expression level was found to be higher on
518 stiff substrate. Since outside-in environmental signal transduction into cellular function converges

519 at the level of transcription, major changes happening in the nucleus could provide important
520 insights into how substrate stiffness is transduced into a proliferation response.

521

522 **Discussion**

523 In this work, we characterized the short time-point, ECM ligand-specific cellular responses of
524 primary human myoblasts cultured on mechanically tuned polyacrylamide-based hydrogels,
525 described the substrate stiffness-specific proteomes of human myoblasts, and reported that
526 nuclear envelope wrinkling can predict myoblast cell cycle state. Our study revealed that FN
527 ligand tethering led to more exacerbated substrate-stiffness-dependent morphological,
528 contractile, and proliferative responses in myoblasts compared to LAM and COL. We reported
529 that the myoblast proteome responds to stiffness by differentially regulating metabolic, Rho
530 cytoskeletal regulation and integrin signaling pathways, with interesting enrichment of nuclear
531 components. Lastly, heavily wrinkled nuclear envelope morphology can predict the absence of
532 Ki67 expression, which can be restored by LPA treatment.

533 The dependence of stiffness-sensing mechanics on ECM ligand is an understudied realm of
534 myogenic cell mechanosensing. ECM ligands bind to specific integrin receptors, which have
535 distinct molecular force transmission mechanics[26]. For example, the FN-integrin α5 bond
536 requires the tension-dependent conformational change of FN to expose a hidden energy site,
537 while COL can bind tension-independently to integrin α2, leading to substrate stiffness-dependent
538 FAK activation on FN-presenting substrates but not those presenting COL[50]. The effects of
539 ECM ligands on myogenic cell stiffness-sensing appear to vary depending on the species and
540 passage number of myogenic cells studied and the specific experimental parameters [17,27,28].
541 In our experiments, we observed that relative to LAM and COL, culturing myoblasts on FN-
542 tethered hydrogels led to more exacerbated stiffness-sensitivity in terms of cell spreading,

543 adhesion alignment, cellular traction, and proliferation. At longer culture time and higher stiffness
544 range, murine MuSCs proliferation have been shown to be stiffness-dependent on both LAM and
545 RGD-presenting hydrogels, while MyoG commitment was stiffness-dependent on RGD and not
546 LAM[17]. Confounding factors to PA hydrogel Young's modulus, such as porosity and ligand
547 tethering density could potentially add to result variability[51,52].

548 The idea that ECM composition could potentially alter myogenic cells mechano-sensitivity is
549 important in the context of in vivo niche ECM remodeling during regeneration, aging and disease.
550 MuSCs niche factors were reported to actively suppress activation pathways to maintain MuSCs
551 quiescence[53,54]. As for LAM, past studies have shown that laminin-2/4 deficiency leads to the
552 loss of integrin α7β1[55], which in turn could disrupt quiescence maintenance[56]. We can
553 therefore infer that the SC connection to LAM via integrin $\alpha 7\beta 1$ is important in preserving SC
554 quiescence, but the exact mechanisms are unknown. In vitro studies on myoblasts, in agreement
555 with other cell types, showed that LAM preferentially activates Rac and suppresses RhoA[57]. In
556 contrast with FN, LAM promotes motile cells with diffused stress fibers and poor vinculin-
557 containing adhesion assembly, characteristic of a high Rac/low RhoA phenotype[58]. These
558 observations are exciting in the context of the Rac-to-Rho switch occurring during MuSCs
559 activation[59]. Rho-regulated cytoskeletal remodeling is critical in cell tension sensing, including
560 matrix stiffness. It is therefore enticing to explore the possibility that LAM actively suppresses
561 MuSCs mechanosensing, while FN enrichment in the injured niche increases MuSCs sensitivity
562 to injury sensation and facilitates the quiescent to proliferative transition, and furthermore, how
563 age- and disease-related irregular ECM deposition impair MuSCs sensitivity to niche remodeling.

564 MuSCs are functionally heterogeneous[60], as are their downstream progenitors. Our results
565 suggested that relatively stiff substrates, tethered with FN, decrease myoblast cell cycle
566 heterogeneity, cultivating a primarily proliferative population. While we observed that soft
567 substrates tethered with FN increased the incidence of Ki67- myoblasts, we did not assess

568 whether the cell cycle itself was impeded. Regarding the split between Ki67+ and Ki67- myoblasts
569 on the same substrate stiffness, our data suggested that perhaps one of the differences between
570 these subpopulations is their contractility, since high Ki67 expression was only observed in the
571 absence of NE wrinkling, a state typically characterized by high cellular contractility[35]. To assess
572 the correlation between cell contractility and NE wrinkling level, we performed traction force
573 microscopy on cells expressing a live Lamin A reporter. To our surprise, cellular traction stress
574 and strain energy were independent of NE wrinkling index, despite pharmacological manipulation
575 of contractility resulting in expected NE wrinkling and Ki67 expression responses. There are a
576 few possible explanations. First, pharmacological manipulation experiments were done on two
577 substrate elasticities while traction force microscopy on Lamin A-GFP expressing cells were
578 conducted exclusively on 17 kPa substrates, so it is possible that cells with wrinkled nuclei on 1
579 kPa had lower traction stresses than cells with wrinkled nuclei on 17 kPa. Second, our proteomic
580 analysis detected a decrease in Lamin A/C on soft substrate, which could potentially take part in
581 increasing NE wrinkling[61,62]. Third, we did not assess nuclear-actin connectivity. If there is a
582 disruption in tension propagation from the cytoskeleton to the nucleus, nuclear tension would be
583 low regardless of cytoskeletal contractility. For example, severing the Linker of Nucleoskeleton
584 and Cytoskeleton (LINC) complex has been shown to induce similar nuclear wrinkling
585 phenotypes[35,63].

586 Whether and how exactly NE wrinkling could suppress proliferation are questions whose pursuit
587 would require the manipulation of NE wrinkling without altering cellular signaling, which is a
588 limitation of the pharmacological strategies that we and others use to manipulate contractility. LPA
589 activates a range of signaling pathways including Ras and Rho/ROCK GTPases which are cell
590 cycle regulators[64–66]. Alternatively, low nuclear tension reduces nucleocytoplasmic exchange
591 of signaling molecules like YAP, cyclin B1, and MyoD by potentially deforming nuclear pore
592 complexes[67–69]. Cosgrove et al. reported a correlation between NE wrinkling and YAP/TAZ

593 nuclear localization in mesenchymal stem cells [35]. In our system, bulk proteomic profiling on
594 soft and stiff substrates did not detect differential YAP target proteins between soft and stiff
595 substrates, suggesting that a YAP/TAZ localization mechanism may not underlie our results.

596 In conclusion, our work emphasized the integrated control of substrate stiffness and ECM
597 composition on myoblast contractility and proliferation, which are heterogeneous phenotypes
598 intimately linked to the NE morphology. The impact of our work extends to biomaterial design
599 applications and implicates fundamental regulation of human myogenic cell mechanosensing.

600 **Acknowledgements**

601 We would like to thank Dr. Qingzong Tseng for advice on the implementation of his TFM ImageJ
602 macros and Dr. Louise Moyle for thoughtful discussions. This work was funded by a Natural
603 Sciences and Engineering Research Council grant to P.M.G. (RGPIN-2019-07144), a Human
604 Frontiers Science Program (RGP0018/2017) to P.M.G. and T.B., a Deutsche
605 Forschungsgemeinschaft (DFG, BE 6270/2-1) to TB, a Connaught International Scholarship to
606 J.N., and a Canada Research Chair in Endogenous Repair to P.M.G. (#950-231201).

607

608 **Author contributions**

609 Conceptualization: J.N., P.M.G.; methodology: J.N., L.W., M.B.; investigation: J.N., L.W., W.L.,
610 Y.H., N.G., C.C.M.; validation and formal analysis: J.N., W.L., L.W., Y.H., N.G.; visualization:
611 J.N., muscle tissue collection and pre-processing: H.A., H.G., R.K.; writing-original draft and
612 writing-review & editing: J.N., P.M.G.; supervision and funding acquisition: T.B., P.M.G. All
613 authors approved the final manuscript.

614

615 **Conflict of Interest**

616 The authors have no conflict of interests that might be perceived to influence the results or
617 discussion reported in this paper.

618

619 ## Figure Legends

620 **Fig 1. Cell spreading area characterization across substrate stiffness and ECM conditions.**
621 **A** Representative confocal images of phalloidin staining in primary human myoblasts cultured for
622 16 hours on 1, 3, 5, or 17 kPa polyacrylamide gels tethered with fibronectin (FN), laminin (LAM),
623 or collagen 1 (COL). Phalloidin-cyan, Hoechst-yellow. scale bar=50 μm **B** Graphs showing mean
624 cell spreading area across hydrogel stiffness, in FN, LAM, and COL conditions, in terms of fold
625 change with respect to the 8 kPa condition (dotted line at y=1). Each data point represents the
626 mean of one biological replicate. n=395-920 cells per condition across N=3 biological replicates.
627 Error bars report mean ± SD. Statistical comparisons were made by two-way ANOVA followed by
628 Tukey's multiple comparison tests.

629

630 **Fig 2. Adhesion alignment characterization across substrate stiffness and ECM conditions.**
631 **A** Representative confocal images of primary human myoblasts adhesion structures 16 hours
632 post-seeding on fibronectin (FN), laminin (LAM) or collagen 1 (COL) tethered polyacrylamide gels.
633 Paxillin-yellow, Hoechst-blue. Scale bar=20 μm. **B** Representative directionality histograms of a
634 paxillin staining ROI with goodness of fit to a Gaussian curve (GoF) = 0.24 (top) and an ROI with
635 GoF=0.84 (bottom). y-axis is the frequency of structures detected by the algorithm and x-axis is
636 the angle direction of those structures with respect to a horizontal line (°) **C** Bar graph showing
637 GoF as a metric of adhesion alignment. Each data point represents the mean of one biological
638 replicate. n=26-32 cells per condition across N=3 biological replicates. Error bars report mean ±
639 SD. Statistical comparisons were made by two-way ANOVA followed by Holm-Šídák multiple
640 comparisons tests.

641

642 **Fig 3. Cellular traction stress measurement across substrate stiffness and ECM**
643 **conditions. A** Representative traction stress maps of myoblasts 16 hours post-seeding on
644 fibronectin (FN), laminin (LAM) or collagen 1 (COL) tethered polyacrylamide gels. Scale bar=20
645 μm **B and C** Bar graphs showing mean and max traction stress, respectively, across substrate
646 stiffness and ECM conditions. n=19-24 cells per condition across N=3 biological replicates. Each
647 data point represents the mean of one biological replicate. Error bars report mean ± SD. Statistical
648 comparisons were made by two-way ANOVA followed by a Holm-Šídák multiple comparison test.
649
650 **Fig 4. Myoblast proliferation exhibits a more linear correlation with stiffness on fibronectin**
651 **(FN) substrates. A** Representative immunostaining images of EdU incorporation assay at 16hr
652 post-seeding on fibronectin (FN), laminin (LAM) or collagen 1 (COL) tethered polyacrylamide gels
653 followed by a 12hr EdU pulse. EdU-yellow, Hoechst-cyan. Scale bar=100 μm. **B** Line graph
654 showing the mean ± SD of % total EdU+ cells. Statistical comparisons were made by two-way
655 ANOVA followed by Holm-Šídák multiple comparison test **C** Linear regression lines of the same
656 data set in B. EdU percentages scaling was conducted by normalizing to the max value of each
657 cell line in order to eliminate cell line variation (scaled $x = x/x_{max}$). Legend displays r^2 (goodness
658 of fit) and p-value testing to determine whether the slope of the fitted line is significantly non-zero.
659 Each data point represents the mean of one biological replicate. n=462-923 cells per condition
660 across N=3 biological replicates.
661
662 **Fig 5. Stiffness-dependent heterogeneity in nuclear envelope wrinkling predicts Ki67**
663 **status. A** Representative confocal images of taut (wrinkle index (WI)≤20) and wrinkled (WI>20)
664 nuclear envelopes. Lamin A/C-cyan. Scale bar=10 μm. **B** Bar graph showing the percentages of
665 taut and wrinkled nuclei on soft and stiff substrates. Each data point represents the mean of one
666 independent technical replicate. Error bars report mean ± SD. n=149-121 cells per condition

667 across N=5 independent experiments on 3 different cell lines. Statistical comparison was made
668 by one-way ANOVA followed by a Holm-Šídák multiple comparison test **C** xy plot with x=WI (%)
669 and y=normalized Ki67 fluorescence intensity (arbitrary unit). Each data point represents one cell.
670 n=180 cells total across N=3 biological replicates **D** Bar graph comparing the percentage of Ki67+
671 nuclei in taut and wrinkled nuclei populations. n=180 cells total across N=3 biological replicates.
672 Statistical comparison was made by a paired one-tail t-test.
673
674 **Fig 6. ML7 and LPA treatments alter myoblast nuclear envelope wrinkling and proliferation.**
675 **A** Representative confocal images of nuclear envelope wrinkling in myoblasts cultured on soft (1
676 kPa) fibronectin-tethered polyacrylamide substrates treated with either DMSO (soft+DMSO) or
677 LPA for 2hr (soft+LPA), and in myoblasts cultured on stiff (17 kPa) fibronectin-tethered substrate
678 treated with either DMSO (stiff+DMSO) or ML7 1hr before fixing (stiff+ML7). Lamin A/C-cyan.
679 Scale bar=10 μm. **B** Bar graph showing the percentages of wrinkled nuclei (WI>20) in
680 soft+DMSO, stiff+DMSO, and stiff+ML7 conditions. n=74-106 cells per condition across N=3
681 biological replicates. **C** Bar graph showing the percentages of wrinkled nuclei in the population of
682 myoblasts cultured in soft+DMSO, stiff+DMSO, and soft+LPA conditions. n=60-72 cells per
683 condition across N=3 biological replicates. **D** Bar graph showing the percentage of Ki67+
684 myoblasts when cells cultured on stiff and soft substrates were treated with, respectively, ML7
685 and LPA, both at 10 μM overnight, in comparison with DMSO controls. n=657-1060 cells across
686 N=3 biological replicates. For all graphs, each data point represents the mean of one biological
687 replicate. Error bars report mean ± SD. Statistical comparison was made by one-way ANOVA
688 followed by a Holm-Šídák multiple comparison test. **E** Representative traction stress maps of a
689 cell with a taut nucleus and a cell with a wrinkled nucleus. Scale bar = 10 μm. **F-G** Bar graph
690 showing the mean and max traction stress of cells with taut and wrinkled nuclei. n=7-9 cells in
691 each condition across two technical replicates of one Lamin A-GFP transduced cell line.

692 **Fig 7. Profiling myoblast proteomes on fibronectin-tethered soft (1 kPa) and stiff (17 kPa)**
693 **culture substrates at 45 hr post-seeding A** Overrepresented PANTHER pathways from the list
694 of differentially expressed proteins upon comparing human myoblasts cultured on soft and stiff
695 fibronectin-tethered polyacrylamide substrates **B** Differentially expressed myogenic-relevant
696 markers **C.** Differentially expressed major cell cycle regulators **D** Differentially expressed proteins
697 with direct ECM interactions **E** Table showing top five enriched cellular components from GO
698 cellular component annotation of proteins upregulated in soft and stiff substrate conditions.
699

700 **S1 Fig. Log-normal cell spreading area distribution A** Frequency distribution of raw,
701 unadjusted myoblast cell spreading areas on 1 kPa fibronectin-tethered polyacrylamide
702 substrates **B** Frequency distribution of the natural log of the same cell spreading area data as in
703 A. **C, D, E** Graphs showing the natural log of myoblast spreading area before normalizing to 9
704 kPa condition. Each data point represents the mean of one biological replicate. n=395-920 cells
705 per condition across N=3 biological replicates. Error bars report mean ± SD.
706

707 **S2 Fig. Viability analysis of myoblasts cultured on fibronectin-tethered polyacrylamide**
708 **substrates.** Representative images of human myoblasts cultured for 16 hours on 1, 3, or 17 kPa
709 fibronectin-tethered polyacrylamide substrates and stained for Hoechst (yellow), propidium iodide
710 (PI; magenta) and Calcein (green). Scale bar=500 μm.
711

712 **S3 Fig. Strain energy of myoblasts across substrate stiffnesses and ECM culture**
713 **conditions.** Bar graph showing strain energy of myoblasts cultured across substrate stiffness
714 and ECM conditions. n=19-24 cells per condition across N=3 biological replicates. Each data point
715 represents the mean of one biological replicate. Error bars report mean ± SD. Statistical
716 comparisons were made by two-way ANOVA followed by a Holm-Šídák multiple comparison test.

717

718 **S4 Fig. Strain energy of myoblasts with taut vs. wrinkled nuclei.** Bar graph showing strain
719 energy of myoblasts having taut (wrinkle index ≤ 20) vs. wrinkled (wrinkle index > 20) nuclei. n=16
720 cells in total across 2 technical replicates. Each data point represents one cell. Error bars report
721 mean ± SD. Statistical comparisons were made by a Student's t-test.

722

723 **S5 Fig. Proteomic profiling of myoblasts cultured on fibronectin-tethered soft (1 kPa) and**
724 **stiff (17 kPa) substrates A** Intensity heat map of all protein groups detected in myoblasts cultured
725 on soft and stiff substrate after filtering by the following criteria: at least 2 of the 3 technical
726 replicate runs have quantitative information; and more than 2100 proteins were quantified **B**
727 Volcano plot showing relative distributions of upregulated proteins in terms of -Log P-value and
728 expression difference (soft-stiff) of all detected proteins. Proteomic analysis was done on one cell-
729 line with 100,000 cells in each stiffness condition, and split into 3 technical replicates.

730

731 **S6 Fig. Expression of metabolic pathway components on soft (1 kPa) and stiff (17 kPa)**
732 **substrate. A** Heat map showing protein levels of metabolic enzymes involved in glycolysis and
733 pentose phosphate pathway in soft and stiff substrates **B** Heat map showing protein levels of ATP
734 synthase subunits on soft and stiff substrates.

735

736 **S7 Fig. Pax7/MyoD analysis of myoblasts cultured on fibronectin-tethered soft (1 kPa) and**
737 **stiff (17 kPa) substrate A** Representative confocal images of myogenic transcription factor
738 immunostaining. Hoechst-grey, Pax7-cyan, MyoD-yellow. Scalebar=20um. **B** Bar graph showing
739 the percentage of cells in each fate category (Pax7-/MyoD+, Pax7+/MyoD+, Pax7+/MyoD-, Pax7-
740 /MyoD-) on soft and stiff substrate. n=435-469 cells across N=3 biological replicates.

741

742 **References**

743 1. Li EW, McKee-Muir OC, Gilbert PM. Chapter Five - Cellular Biomechanics in Skeletal
744 Muscle Regeneration. In: Sassoon D, editor. Current Topics in Developmental Biology.
745 Academic Press; 2018. pp. 125–176. doi:10.1016/bs.ctdb.2017.08.007

746 2. Loreti M, Sacco A. The jam session between muscle stem cells and the extracellular matrix
747 in the tissue microenvironment. Npj Regen Med. 2022;7: 1–15. doi:10.1038/s41536-022-
748 00204-z

749 3. Silver JS, Günay KA, Cutler AA, Vogler TO, Brown TE, Pawlikowski BT, et al. Injury-
750 mediated stiffening persistently activates muscle stem cells through YAP and TAZ
751 mechanotransduction. Sci Adv. 2021;7: eabe4501. doi:10.1126/sciadv.abe4501

752 4. Lacraz G, Rouleau AJ, Couture V, Söllrald T, Drouin G, Veillette N, et al. Increased
753 stiffness in aged skeletal muscle impairs muscle progenitor cell proliferative activity. PLoS
754 ONE. 2015;10: 1–13. doi:10.1371/journal.pone.0136217

755 5. Trensz F, Lucien F, Couture V, Söllrald T, Drouin G, Rouleau AJ, et al. Increased
756 microenvironment stiffness in damaged myofibers promotes myogenic progenitor cell
757 proliferation. Skelet Muscle. 2015;5: 1–16. doi:10.1186/s13395-015-0030-1

758 6. Stearns-Reider KM, D'Amore A, Beezhold K, Rothrauff B, Cavalli L, Wagner WR, et al.
759 Aging of the skeletal muscle extracellular matrix drives a stem cell fibrogenic conversion.
760 Aging Cell. 2017;16: 518–528. doi:10.1111/acel.12578

761 7. Blanpied P, Smidt GL. The Difference in Stiffness of the Active Plantarflexors Between
762 Young and Elderly Human Females. J Gerontol. 1993;48: M58–M63.
763 doi:10.1093/geronj/48.2.M58

764 8. Wood LK, Kayupov E, Gumucio JP, Mendias CL, Claflin DR, Brooks SV. Intrinsic stiffness
765 of extracellular matrix increases with age in skeletal muscles of mice. J Appl Physiol.
766 2014;117: 363–369. doi:10.1152/japplphysiol.00256.2014

767 9. Alnaqeeb MA, Al Zaid NS, Goldspink G. Connective tissue changes and physical
768 properties of developing and ageing skeletal muscle. J Anat. 1984;139: 677–689.

769 10. Measuring changes in muscle stiffness after eccentric exercise using elastography - Green
770 - 2012 - NMR in Biomedicine - Wiley Online Library. [cited 6 Feb 2023]. Available:
771 https://analyticalsciencejournals.onlinelibrary.wiley.com/doi/full/10.1002/nbm.1801?casa_to
772 ken=d2zuGJ30wkEAAAAA%3A7APVAtrFf9qMwz_o4a4cXzzH9ltS_OLw4Jf6pHIQJaVdK6
773 dVPRmDK16OOzVHdKbOJkbQl5cQWFUpNQ

774 11. Lacourpaille L, Gross R, Hug F, Guével A, Péréon Y, Magot A, et al. Effects of Duchenne
775 muscular dystrophy on muscle stiffness and response to electrically-induced muscle
776 contraction: A 12-month follow-up. Neuromuscul Disord. 2017;27: 214–220.
777 doi:10.1016/j.nmd.2017.01.001

778 12. Lacourpaille L, Hug F, Guével A, Péréon Y, Magot A, Hogrel J-Y, et al. Non-invasive
779 assessment of muscle stiffness in patients with duchenne muscular dystrophy. Muscle
780 Nerve. 2015;51: 284–286. doi:10.1002/mus.24445

781 13. Engler AJ, Griffin MA, Sen S, Bönnemann CG, Sweeney HL, Discher DE. Myotubes
782 differentiate optimally on substrates with tissue-like stiffness: Pathological implications for
783 soft or stiff microenvironments. J Cell Biol. 2004. doi:10.1083/jcb.200405004

784 14. Stedman HH, Sweeney HL, Shrager JB, Maguire HC, Panettieri RA, Petrof B, et al. The
785 mdx mouse diaphragm reproduces the degenerative changes of Duchenne muscular
786 dystrophy. Nature. 1991;352: 536–539. doi:10.1038/352536a0

787 15. Monge C, Distasio N, Rossi T, Sébastien M, Sakai H, Kalman B, et al. Quiescence of
788 human muscle stem cells is favored by culture on natural biopolymeric films. 2017; 1–13.
789 doi:10.1186/s13287-017-0556-8

790 16. Boontheekul T, Hill EE, Kong HJ, Mooney DJ. Regulating myoblast phenotype through
791 controlled gel stiffness and degradation. Tissue Eng. 2007;13: 1431–1442.
792 doi:10.1089/ten.2006.0356

793 17. Madl CM, Flaig IA, Holbrook CA, Wang YX, Blau HM. Biophysical matrix cues from the
794 regenerating niche direct muscle stem cell fate in engineered microenvironments.
795 Biomaterials. 2021;275: 120973. doi:10.1016/j.biomaterials.2021.120973

796 18. Bauer A, Gu L, Kwee B, Li WA, Dellacherie M, Celiz AD, et al. Hydrogel substrate stress-
797 relaxation regulates the spreading and proliferation of mouse myoblasts. Acta Biomater.
798 2017. doi:10.1016/j.actbio.2017.08.041

799 19. Bunney PE, Zink AN, Holm AA, Billington CJ, Kotz CM. Hydrogel substrate stress-
800 relaxation regulates the spreading and proliferation of mouse myoblasts. Physiol Behav.
801 2017;176: 139–148. doi:10.1016/j.physbeh.2017.03.040

802 20. Gilbert PM, Havenstrite KL, Magnusson KEG, Sacco A, Leonardi NA, Kraft P, et al.
803 Substrate elasticity regulates skeletal muscle stem cell self-renewal in culture. Science.
804 2010;329: 1078–1081. doi:10.1126/science.1191035

805 21. Moyle LA, Cheng RY, Liu H, Davoudi S, Ferreira SA, Nissar AA, et al. Three-dimensional
806 niche stiffness synergizes with Wnt7a to modulate the extent of satellite cell symmetric
807 self-renewal divisions.

808 22. Brzóska E, Bello V, Darribère T, Moraczewski J. Integrin α3 subunit participates in
809 myoblast adhesion and fusion in vitro. Differentiation. 2006;74: 105–118.
810 doi:10.1111/j.1432-0436.2005.00059.x

811 23. Wilschut KJ, van Tol HTA, Arkesteijn GJA, Haagsman HP, Roelen BAJ. Alpha 6 integrin is
812 important for myogenic stem cell differentiation. Stem Cell Res. 2011;7: 112–123.
813 doi:10.1016/j.scr.2011.05.001

814 24. Rayagiri SS, Ranaldi D, Raven A, Mohamad Azhar NIF, Lefebvre O, Zammit PS, et al.
815 Basal lamina remodeling at the skeletal muscle stem cell niche mediates stem cell self-
816 renewal. Nat Commun. 2018;9: 1–12. doi:10.1038/s41467-018-03425-3

817 25. Gullberg D, Velling T, Lohikangas L, Tiger C-F. Integrins During Muscle Development and
818 in Muscular Dystrophies. Pediatr Pathol Mol Med. 1998;18: 303–327.
819 doi:10.1080/15513819809168793

820 26. Seetharaman S, Etienne-Manneville S. Integrin diversity brings specificity in
821 mechanotransduction. Biol Cell. 2018;110: 49–64. doi:10.1111/boc.201700060

822 27. Calve S, Simon H-G. Biochemical and mechanical environment cooperatively regulate
823 skeletal muscle regeneration. FASEB J. 2012;26: 2538. doi:10.1096/FJ.11-200162

824 28. Boonen KJM, Rosaria-Chak KY, Baaijens FPT, van der Schaft DWJ, Post MJ. Essential
825 environmental cues from the satellite cell niche: optimizing proliferation and differentiation.
826 Am J Physiol-Cell Physiol. 2009;296: C1338–C1345. doi:10.1152/ajpcell.00015.2009

827 29. Tse JR, Engler AJ. Preparation of Hydrogel Substrates with Tunable Mechanical
828 Properties. Curr Protoc Cell Biol. 2010;47: 10.16.1-10.16.16.
829 doi:10.1002/0471143030.cb1016s47

830 30. Afshar ME, Abraha HY, Bakooshli MA, Davoudi S, Thavandiran N, Tung K, et al. A 96-well
831 culture platform enables longitudinal analyses of engineered human skeletal muscle
832 microtissue strength. Sci Rep. 2020;10: 6918. doi:10.1038/s41598-020-62837-8

833 31. Afshar Bakooshli M, Lippmann ES, Mulcahy B, Iyer N, Nguyen CT, Tung K, et al. A 3D
834 culture model of innervated human skeletal muscle enables studies of the adult
835 neuromuscular junction. Brack A, Bronner ME, Brack A, editors. eLife. 2019;8: e44530.
836 doi:10.7554/eLife.44530

837 32. Pelham RJ, Wang Y. Cell locomotion and focal adhesions are regulated by
838 substrate flexibility. Proc Natl Acad Sci. 1997;94: 13661–13665.
839 doi:10.1073/pnas.94.25.13661

840 33. Martiel JL, Leal A, Kurzawa L, Balland M, Wang I, Vignaud T, et al. Measurement of cell
841 traction forces with ImageJ. Methods Cell Biol. 2015;125: 269–287.
842 doi:10.1016/bs.mcb.2014.10.008

843 34. Tseng Q, Duchemin-Pelletier E, Deshiere A, Balland M, Guillou H, Filhol O, et al. Spatial
844 organization of the extracellular matrix regulates cell–cell junction positioning. Proc Natl
845 Acad Sci. 2012;109: 1506–1511. doi:10.1073/pnas.1106377109

846 35. Cosgrove BD, Loebel C, Driscoll TP, Tsinman TK, Dai EN, Heo SJ, et al. Nuclear envelope
847 wrinkling predicts mesenchymal progenitor cell mechano-response in 2D and 3D
848 microenvironments. Biomaterials. 2021;270: 120662.
849 doi:10.1016/J.BIOMATERIALS.2021.120662

850 36. Iggo R. Lentiviral Transduction of Mammary Epithelial Cells. In: Vivanco M dM., editor.
851 Mammary Stem Cells: Methods and Protocols. New York, NY: Springer US; 2022. pp.
852 159–183. doi:10.1007/978-1-0716-2193-6_8

853 37. Schormann W, Hariharan S, Andrews DW. A reference library for assigning protein
854 subcellular localizations by image-based machine learning. J Cell Biol. 2020;219:
855 e201904090. doi:10.1083/jcb.201904090

856 38. Horzum U, Ozdil B, Pesen-Okvur D. Step-by-step quantitative analysis of focal adhesions.
857 MethodsX. 2014;1: 56–59. doi:10.1016/j.mex.2014.06.004

858 39. Urciuolo A, Quarta M, Morbidoni V, Gattazzo F, Molon S, Grumati P, et al. Collagen VI
859 regulates satellite cell self-renewal and muscle regeneration. Nat Commun. 2013;4: 1964.
860 doi:10.1038/ncomms2964

861 40. Safaee H, Bakooshli MA, Davoudi S, Cheng RY, Martowirogo AJ, Li EW, et al. Tethered
862 Jagged-1 Synergizes with Culture Substrate Stiffness to Modulate Notch-Induced
863 Myogenic Progenitor Differentiation. Cell Mol Bioeng. 2017;10: 501–513.
864 doi:10.1007/s12195-017-0506-7

865 41. Geiger B, Spatz JP, Bershadsky AD. Environmental sensing through focal adhesions. Nat
866 Rev Mol Cell Biol. 2009;10: 21–33. doi:10.1038/nrm2593

867 42. Wu C, Asokan SB, Berginski ME, Haynes EM, Sharpless NE, Griffith JD, et al. Arp2/3 Is
868 Critical for Lamellipodia and Response to Extracellular Matrix Cues but Is Dispensable for
869 Chemotaxis. Cell. 2012;148: 973–987. doi:10.1016/j.cell.2011.12.034

870 43. The small GTPase RhoG regulates microtubule-mediated focal adhesion disassembly |
871 Scientific Reports. [cited 7 Feb 2023]. Available: https://www.nature.com/articles/s41598-
872 019-41558-7

873 44. Bruno S, Crissman HA, Bauer KD, Darzynkiewicz Z. Changes in cell nuclei during S
874 Phase: Progressive chromatin condensation and altered expression of the proliferation-
875 associated nuclear proteins Ki-67, cyclin (PCNA), p105, and p34. Exp Cell Res. 1991;196:
876 99–106. doi:10.1016/0014-4827(91)90460-C

877 45. Gomes ER, Jani S, Gundersen GG. Nuclear Movement Regulated by Cdc42, MRCK,
878 Myosin, and Actin Flow Establishes MTOC Polarization in Migrating Cells. Cell. 2005;121:
879 451–463. doi:10.1016/j.cell.2005.02.022

880 46. Swaminathan V, Kalappurakkal JM, Mehta SB, Nordenfelt P, Moore TI, Koga N, et al. Actin
881 retrograde flow actively aligns and orients ligand-engaged integrins in focal adhesions.
882 Proc Natl Acad Sci. 2017;114: 10648–10653. doi:10.1073/pnas.1701136114

883 47. Vogel V, Sheetz M. Local force and geometry sensing regulate cell functions. Nat Rev Mol
884 Cell Biol. 2006;7: 265–275. doi:10.1038/nrm1890

885 48. Tilghman RW, Blais EM, Cowan CR, Sherman NE, Grigera PR, Jeffery ED, et al. Matrix
886 rigidity regulates cancer cell growth by modulating cellular metabolism and protein
887 synthesis. PloS One. 2012;7: e37231. doi:10.1371/journal.pone.0037231

888 49. Li L, Chambard JC, Karin M, Olson EN. Fos and Jun repress transcriptional activation by
889 myogenin and MyoD: the amino terminus of Jun can mediate repression. Genes Dev.
890 1992;6: 676–689. doi:10.1101/gad.6.4.676

891 50. Seong J, Tajik A, Sun J, Guan J-L, Humphries MJ, Craig SE, et al. Distinct biophysical
892 mechanisms of focal adhesion kinase mechanoactivation by different extracellular matrix
893 proteins. Proc Natl Acad Sci U S A. 2013;110: 19372–19377.
894 doi:10.1073/pnas.1307405110

895 51. Trappmann B, Gautrot JE, Connelly JT, Strange DGT, Li Y, Oyen ML, et al. Extracellular-
896 matrix tethering regulates stem-cell fate. Nat Mater 2012 117. 2012;11: 642–649.
897 doi:10.1038/nmat3339

898 52. Wen JH, Vincent LG, Fuhrmann A, Choi YS, Hribar K, Taylor-Weiner H, et al. Interplay of
899 Matrix Stiffness and Protein Tethering in Stem Cell Differentiation. Nat Mater. 2014;13:
900 979. doi:10.1038/nmat4051

901 53. Baghdadi MB, Castel D, Machado L, Fukada S, Birk DE, Relaix F, et al. Reciprocal
902 signalling by Notch–Collagen V–CALCR retains muscle stem cells in their niche. Nature.
903 2018;557: 714–718. doi:10.1038/s41586-018-0144-9

904 54. Zhang L, Noguchi Y, Nakayama H, Kaji T, Tsujikawa K, Ikemoto-Uezumi M, et al. The
905 CalcR-PKA-Yap1 Axis Is Critical for Maintaining Quiescence in Muscle Stem Cells. Cell
906 Rep. 2019;29: 2154-2163.e5. doi:10.1016/j.celrep.2019.10.057

907 55. Vachon PH, Xu H, Liu L, Loechel F, Hayashi Y, Arahata K, et al. Integrins (␣7␤1) in
908 Muscle Function and Survival.

909 56. Rozo M, Li L, Fan CM. Targeting β1-integrin signaling enhances regeneration in aged and
910 dystrophic muscle in mice. Nat Med. 2016;22: 889–896. doi:10.1038/nm.4116

911 57. Gu J, Sumida Y, Sanzen N, Sekiguchi K. Laminin-10/11 and Fibronectin Differentially
912 Regulate Integrin- dependent Rho and Rac Activation via p130Cas-CrkII-DOCK180
913 Pathway *. J Biol Chem. 2001;276: 27090–27097. doi:10.1074/jbc.M102284200

914 58. Goodman SL, Risse G, von der Mark K. The E8 subfragment of laminin promotes
915 locomotion of myoblasts over extracellular matrix. J Cell Biol. 1989;109: 799–809.
916 doi:10.1083/jcb.109.2.799

917 59. Kann AP, Hung M, Wang W, Nguyen J, Gilbert PM, Wu Z, et al. An injury-responsive Rac-
918 to-Rho GTPase switch drives activation of muscle stem cells through rapid cytoskeletal
919 remodeling. Cell Stem Cell. 2022;29: 933-947.e6. doi:10.1016/j.stem.2022.04.016

920 60. Tierney MT, Sacco A. Satellite Cell Heterogeneity in Skeletal Muscle Homeostasis. Trends
921 Cell Biol. 2016;26: 434–444. doi:10.1016/J.TCB.2016.02.004

922 61. Buxboim A, Irianto J, Swift J, Athirasala A, Shin JW, Rehfeldt F, et al. Coordinated
923 increase of nuclear tension and lamin-A with matrix stiffness outcompetes lamin-B receptor
924 that favors soft tissue phenotypes. Mol Biol Cell. 2017;28: 3333–3348.
925 doi:10.1091/MBC.E17-06-0393/ASSET/IMAGES/LARGE/3333FIG8.TIF.GZ.JPEG

926 62. Kim J-K, Louhghalam A, Lee G, Schafer BW, Wirtz D, Kim D-H. Nuclear lamin A/C
927 harnesses the perinuclear apical actin cables to protect nuclear morphology. Nat Commun.
928 2017;8: 2123. doi:10.1038/s41467-017-02217-5

929 63. Dantas M, Oliveira A, Aguiar P, Maiato H, Ferreira JG. Nuclear tension controls mitotic
930 entry by regulating cyclin B1 nuclear translocation. J Cell Biol. 2022;221: e202205051.
931 doi:10.1083/jcb.202205051

932 64. Mills GB, Moolenaar WH. The emerging role of lysophosphatidic acid in cancer. Nat Rev
933 Cancer. 2003;3: 582–591. doi:10.1038/nrc1143

934 65. Manning Jr. TJ, Rosenfeld SS, Sontheimer H. Lysophosphatidic acid stimulates
935 actomyosin contraction in astrocytes. J Neurosci Res. 1998;53: 343–352.
936 doi:10.1002/(SICI)1097-4547(19980801)53:3<343::AID-JNR8>3.0.CO;2-A

937 66. Lin M-E, Herr DR, Chun J. Lysophosphatidic acid (LPA) receptors: signaling properties and
938 disease relevance. Prostaglandins Other Lipid Mediat. 2010;91: 130–138.
939 doi:10.1016/j.prostaglandins.2009.02.002

940 67. Elosegui-Artola A, Andreu I, Beedle AEM, Lezamiz A, Uroz M, Kosmalska AJ, et al. Force
941 Triggers YAP Nuclear Entry by Regulating Transport across Nuclear Pores. Cell.
942 2017;171: 1397-1410.e14. doi:10.1016/J.CELL.2017.10.008

943 68. Andreu I, Granero-Moya I, Chahare NR, Clein K, Molina-Jordán M, Beedle AEM, et al.
944 Mechanical force application to the nucleus regulates nucleocytoplasmic transport. Nat
945 Cell Biol. 2022;24: 896–905. doi:10.1038/s41556-022-00927-7

946 69. Jacchetti E, Nasehi R, Boeri L, Parodi V, Negro A, Albani D, et al. The nuclear import of
947 the transcription factor MyoD is reduced in mesenchymal stem cells grown in a 3D micro-
948 engineered niche. Sci Rep 2021 111. 2021;11: 1–19. doi:10.1038/s41598-021-81920-2

949

Fig 1.

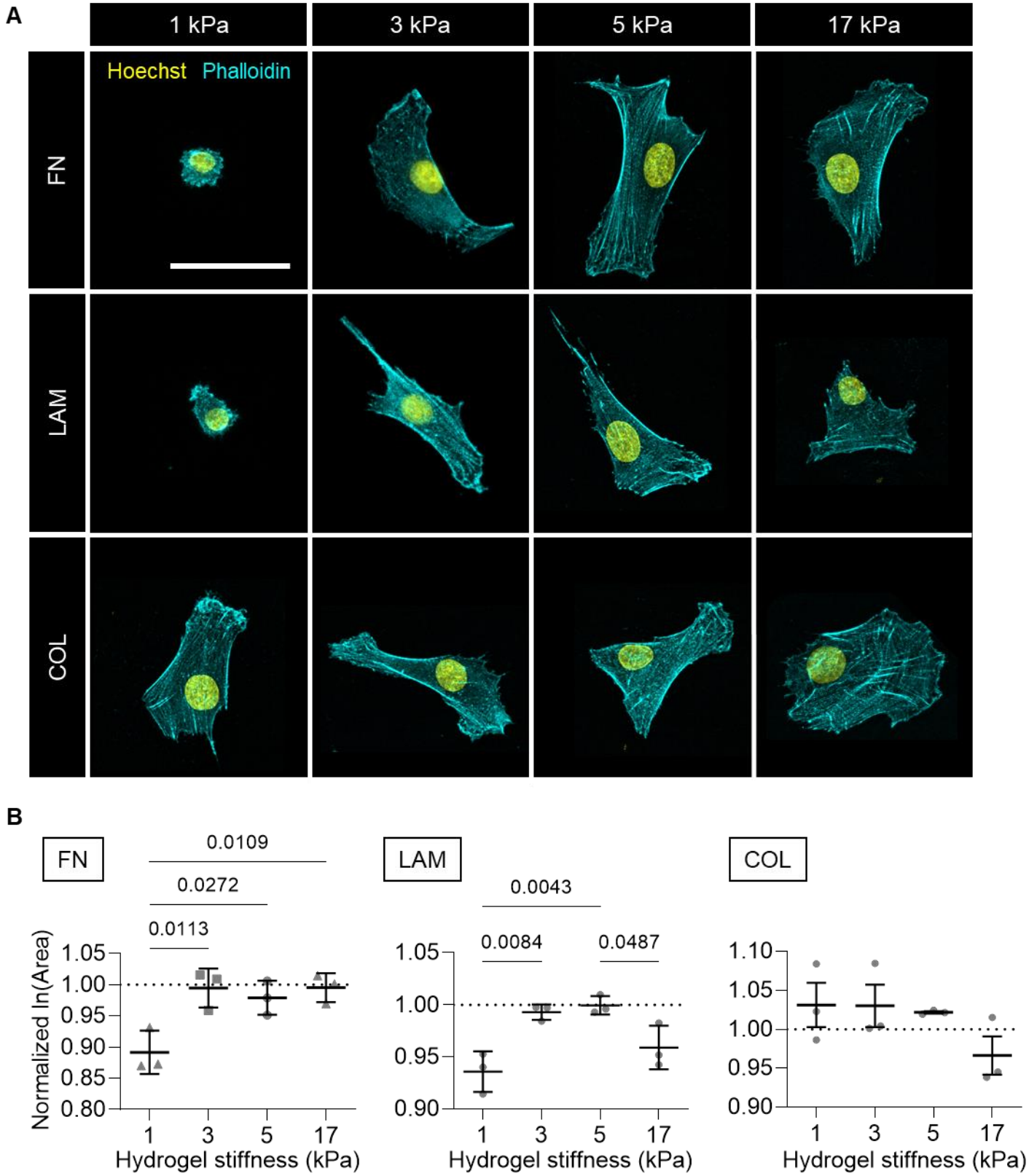
A
1 kPa
3 kPa
5 kPa
17 kPa
Hoechst
Phalloidin
FN
LAM
COL
B
FN
0.0109
0.0272
0.0113
Normalized ln(Area)
1.05
1.00
0.95
0.90
0.85
0.80
1
3
5
17
Hydrogel stiffness (kPa)
LAM
0.0043
0.0084
0.0487
1.05
1.00
0.95
0.90
1
3
5
17
Hydrogel stiffness (kPa)
COL
1.10
1.05
1.00
0.95
0.90
1
3
5
17
Hydrogel stiffness (kPa)

Fig 2.

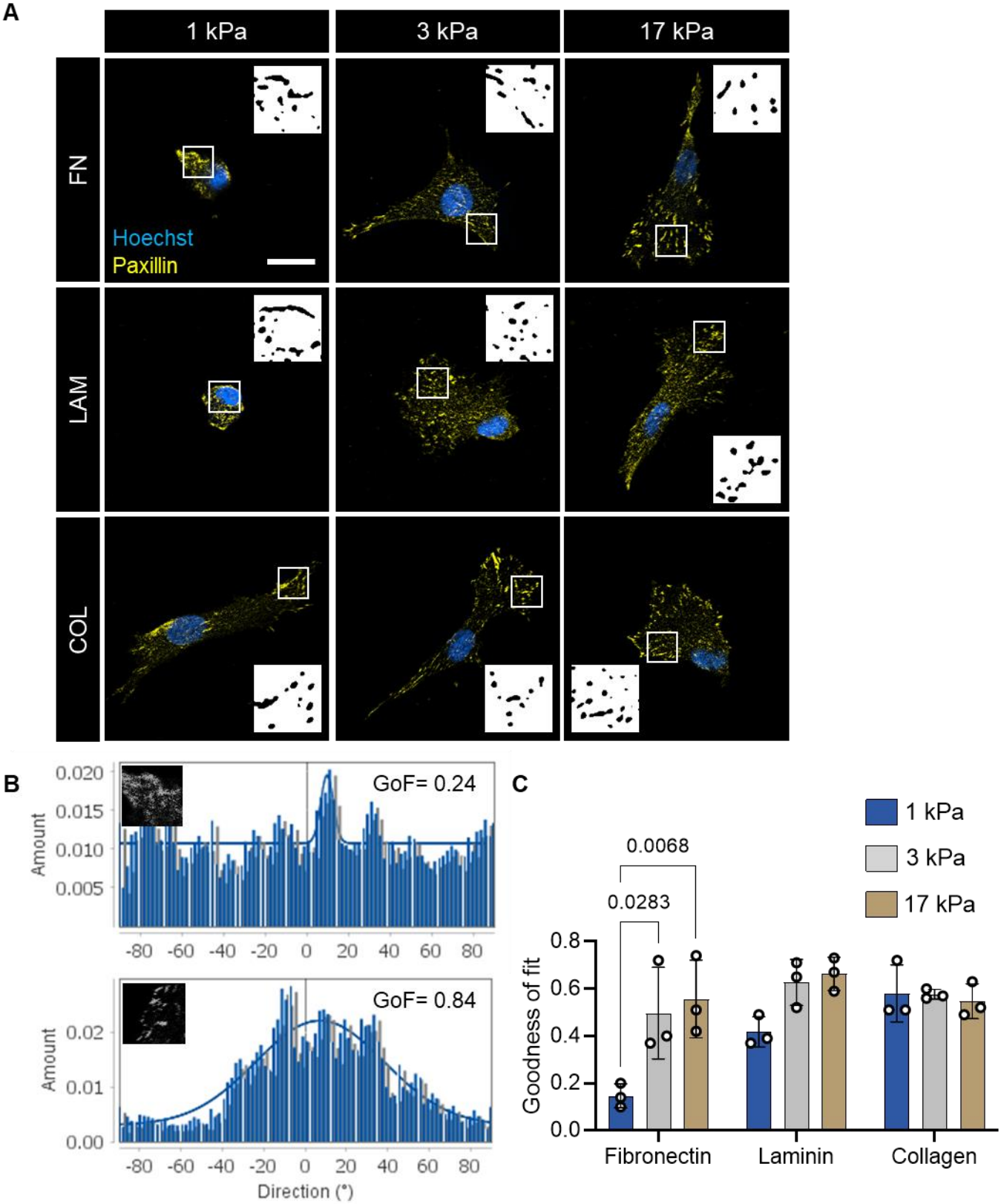
A
1 kPa
3 kPa
17 kPa
FN
LAM
COL
Hoechst
Paxillin
B
GoF= 0.24
GoF= 0.84
Amount
Direction (°)
C
1 kPa
3 kPa
17 kPa
0.0068
0.0283
Goodness of fit
Fibronectin
Laminin
Collagen

Fig 3.

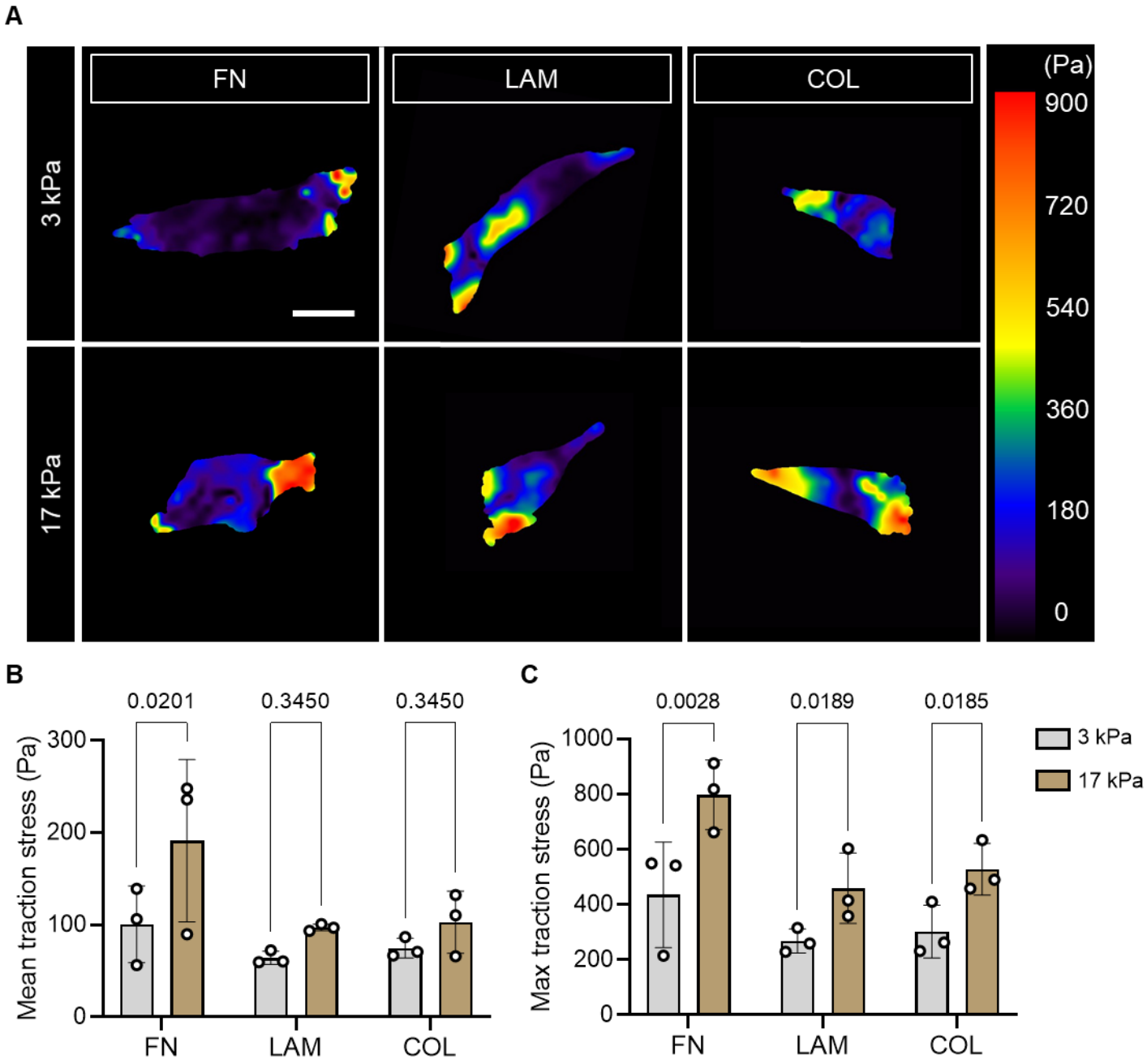
A
FN
LAM
COL
3 kPa
17 kPa
(Pa)
900
720
540
360
180
0
B
0.0201
0.3450
0.3450
Mean traction stress (Pa)
300
200
100
0
FN
LAM
COL
C
0.0028
0.0189
0.0185
Max traction stress (Pa)
1000
800
600
400
200
0
FN
LAM
COL
3 kPa
17 kPa

Fig 4.

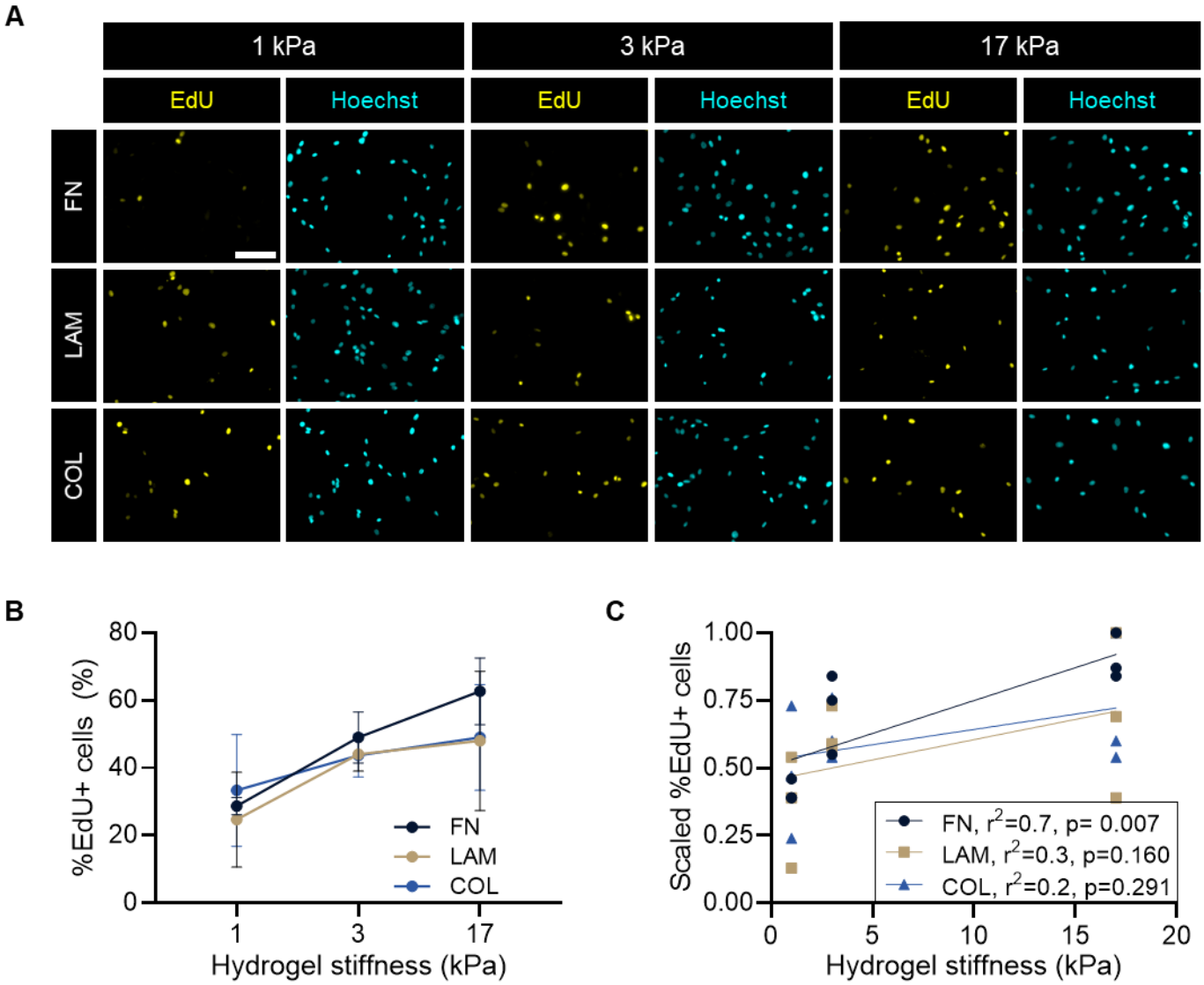
A
1 kPa
3 kPa
17 kPa
EdU
Hoechst
FN
LAM
COL
B
%EdU+ cells (%)
Hydrogel stiffness (kPa)
FN
LAM
COL
C
Scaled %EdU+ cells
Hydrogel stiffness (kPa)
FN, r2=0.7, p= 0.007
LAM, r2=0.3, p=0.160
COL, r2=0.2, p=0.291

Fig 5.

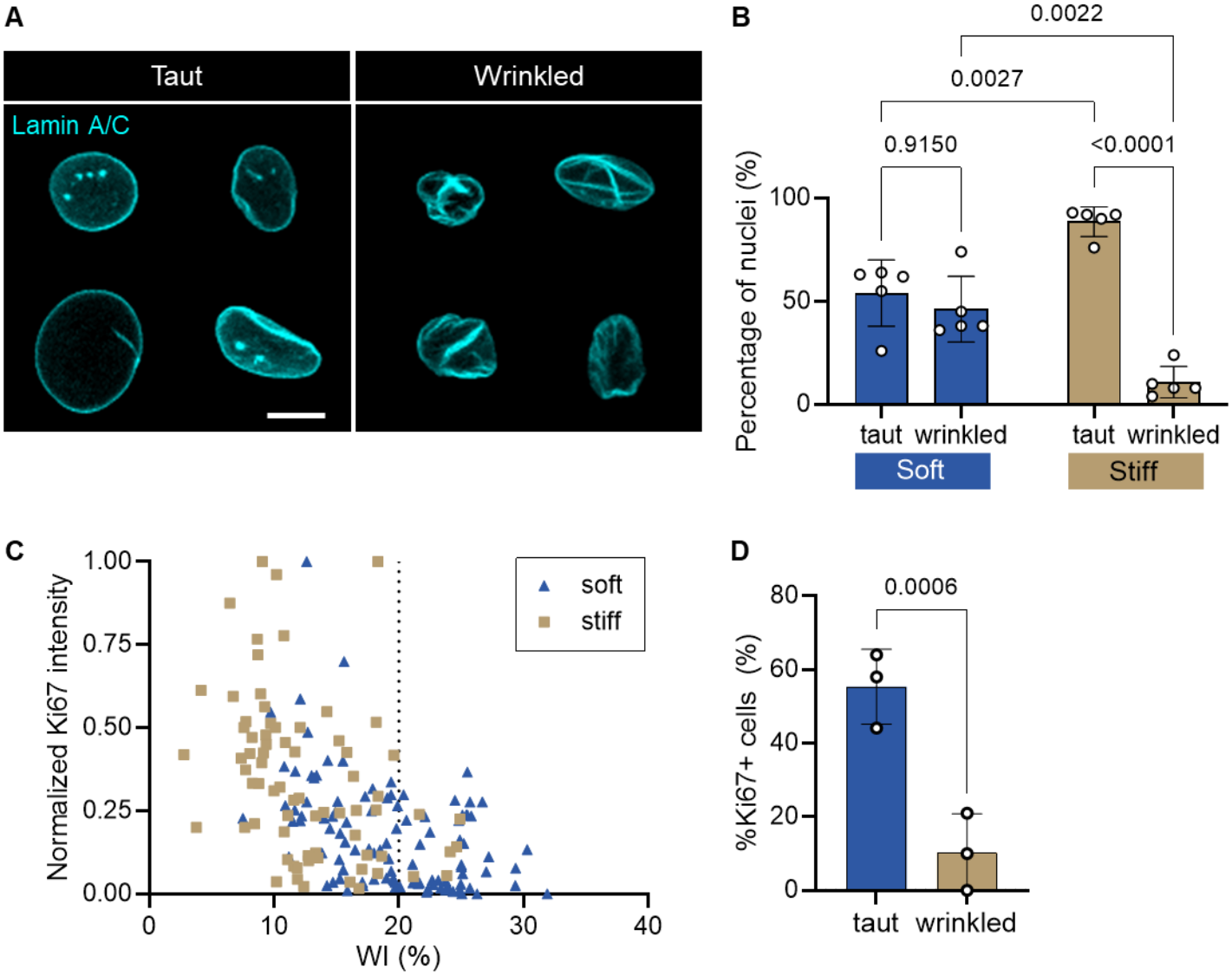
A
Taut
Wrinkled
Lamin A/C
B
0.0022
0.0027
0.9150
<0.0001
Percentage of nuclei (%)
100
50
0
taut
wrinkled
taut
wrinkled
Soft
Stiff
C
Normalized Ki67 intensity
1.00
0.75
0.50
0.25
0.00
0
10
20
30
40
WI (%)
soft
stiff
D
%Ki67+ cells (%)
80
60
40
20
0
0.0006
taut
wrinkled

Fig 6.

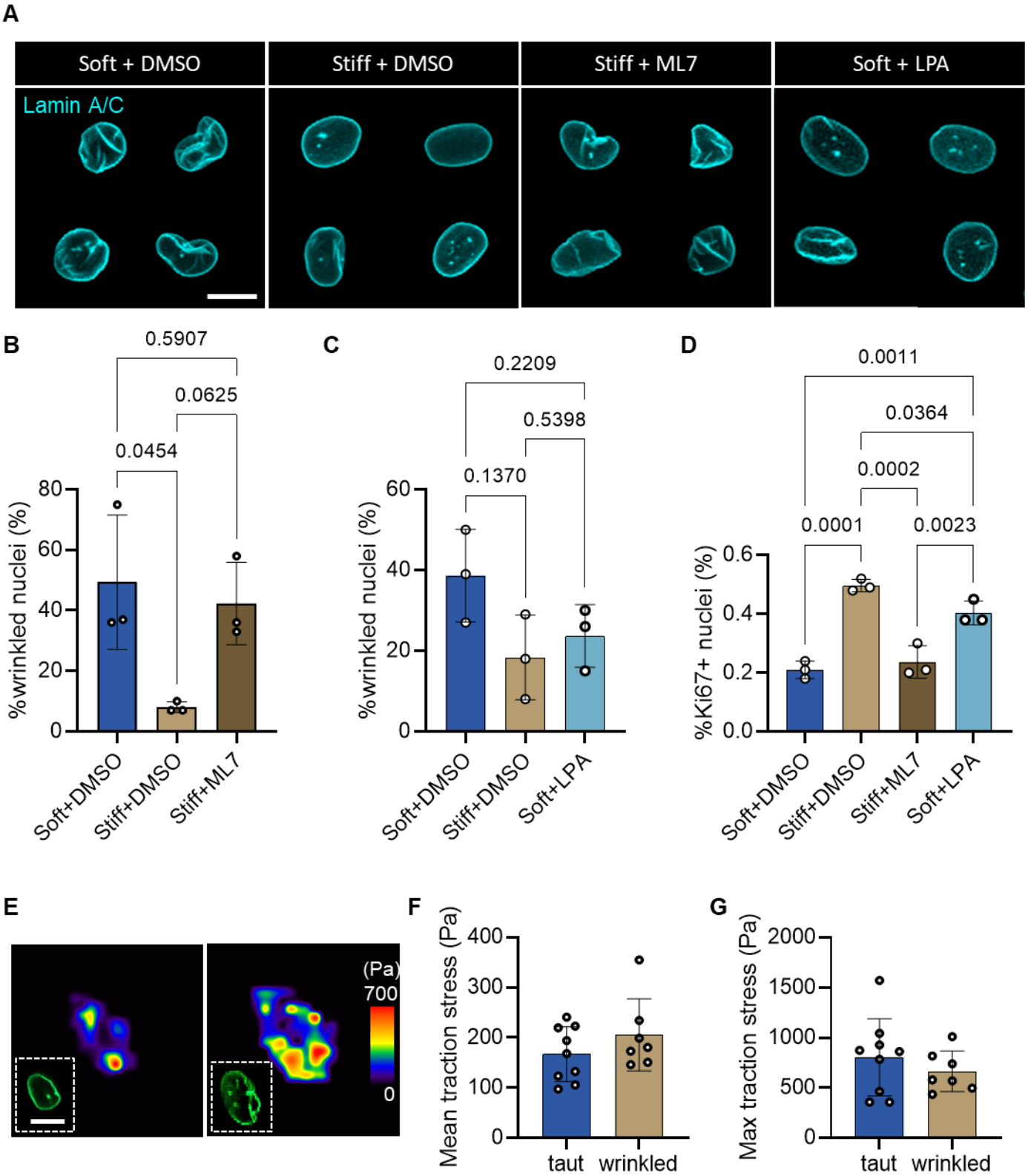
A
Soft + DMSO
Stiff + DMSO
Stiff + ML7
Soft + LPA
Lamin A/C
B
0.5907
0.0625
0.0454
%wrinkled nuclei (%)
80
60
40
20
0
Soft+DMSO
Stiff+DMSO
Stiff+ML7
C
0.2209
0.5398
0.1370
%wrinkled nuclei (%)
60
40
20
0
Soft+DMSO
Stiff+DMSO
Soft+LPA
D
0.0011
0.0364
0.0002
0.0001
0.0023
%Ki67+ nuclei (%)
0.6
0.4
0.2
0.0
Soft+DMSO
Stiff+DMSO
Stiff+ML7
Soft+LPA
E
(Pa)
700
0
F
Mean traction stress (Pa)
400
300
200
100
0
taut
wrinkled
G
Max traction stress (Pa)
2000
1500
1000
500
0
taut
wrinkled

Fig 7.

A

PANTHER pathways	# genes	Fold enrichment	Raw P-value
Pentose phosphate pathway	4	11.28	1.11E-03
Glycolysis	8	10.15	6.51E-06
Integrin signaling pathway	27	3.43	1.55E-07
Cytoskeletal regulation by Rho GTPase	11	3.25	1.11E-03
Huntington disease	15	2.51	1.76E-03
Unclassified	666	0.94	3.74E-05

B

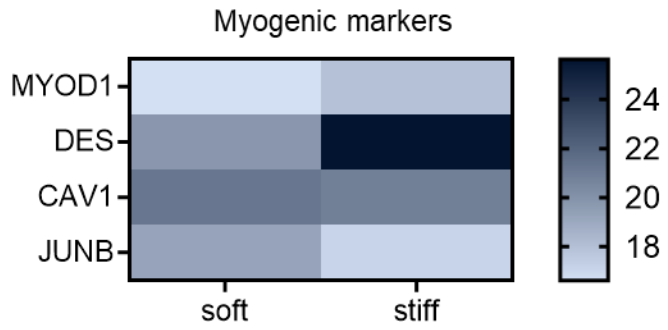

C

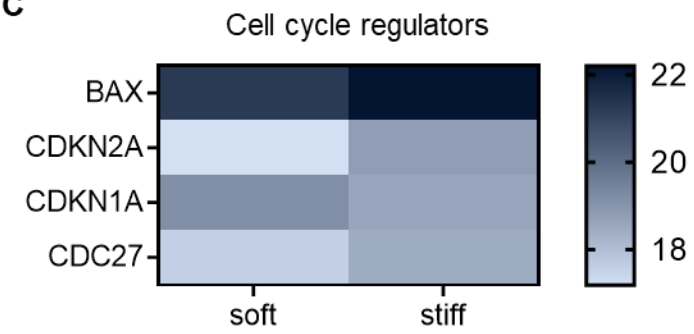

D

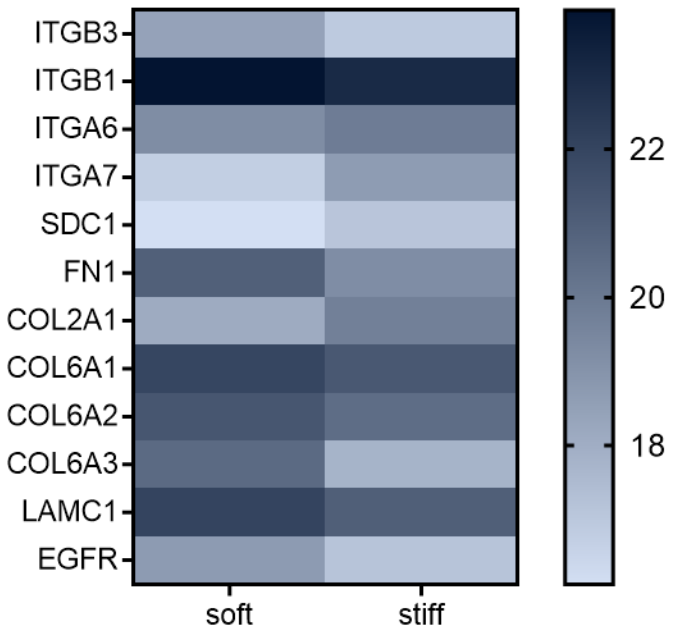

E

GO cellular component enrichment

Upregulated in soft condition	Upregulated in stiff condition
Ribonucleoprotein complex	Nucleus
Membrane-enclosed lumen	Nucleoplasm
Intracellular organelle lumen	Nuclear lumen
Nucleolus	Ribonucleoprotein complex
Organelle lumen	Intracellular organelle